Proceedings of PSFVIP-3
March 18-21, 2001, Maui, Hawaii, U.S.A
F3003

OH LIF in Atmospheric Pressure Flames Excited by a Tunable OPO (Type II) Laser System

R. Stocker, J. Karl, and D. Hein

Lehrstuhl für Thermische Kraftanlagen, Technische Universität München
D-85747 Garching, Boltzmannstr. 15, Germany
E-mail: stocker@ltk.mw.tum.de

ABSTRACT: One of the most important molecules in analysing combustion processes is the OH radical, which provides information about combustion kinetics, flame front etc. With the laser induced fluorescence (LIF) technique the hydroxyl radical can be detected in flames. The paper shows possibilities of OH detection with a tunable OPO (Type II) laser system in flame research. Rotational lines of the hydroxyl radical within the A-X (0,0), (1,0), (2,0) and (3,0) bands have been excited and thus identified. The rotational lines of the OH A-X (0,0), (1,0) and (2,0) bands can be used for selective OH detection. The OH LIF signal intensities are sufficient to obtain 2-dimensional time-resolved qualitative OH distribution measurements.

KEYWORDS: OH, LIF, Fluorescence, Combustion, OPO

1. INTRODUCTION

Laser induced fluorescence (LIF) is a well-known technique to detect molecules, like O_2, NO or OH, in combustion processes. It is highly selective, sensitive and non-intrusive. Pulsed-laser planar imaging allows resolution of species in space and time. One of the most important molecules in analysing combustion processes is the OH radical, which provides information about combustion kinetics, flame front etc. A detailed understanding of gas-dynamic processes is important for the engineering design of burners to increase efficiency and to minimize pollutants from combustion (Rothe and Andresen, 1996; Kohse-Höinghaus, 1994; Eckbreth, 1996).
In the excitation wavelength range from 325 nm down to 240 nm (30,769 cm^{-1} to 41,667 cm^{-1}) transitions within the OH $A^2\Sigma^+ \leftarrow X^2\Pi$ (0,0), (1,0), (2,0) and (3,0) bands have been detected. Brockhinke et al., 1999, and Dreizler et al., 1993, describe the excitation of OH ($A^2\Sigma^+$), v' = 1 in atmospheric pressure flames. LIF measurements of turbulent premixed flames in a high-pressure environment are shown by Kobayashi et al., 1999. Laser-induced fluorescence detection of the OH ($A^2\Sigma^+$), v' = 2 transition in atmospheric pressure flames are described by Versluis et al., 1994, and Bormann et al., 1997. The visualization and detection of hydroxyl radicals in various flames with excitation of OH ($A^2\Sigma^+$), v' = 3 transition were applied by Arnold et al., 1990, Koch et al., 1993, Rothe et al., 1994, and Frodermann, 1996. The detection of OH in a large scale facility are presented by Versluis et al., 1992, by laser-induced fluorescence imaging in a 100 kW natural gas flame.

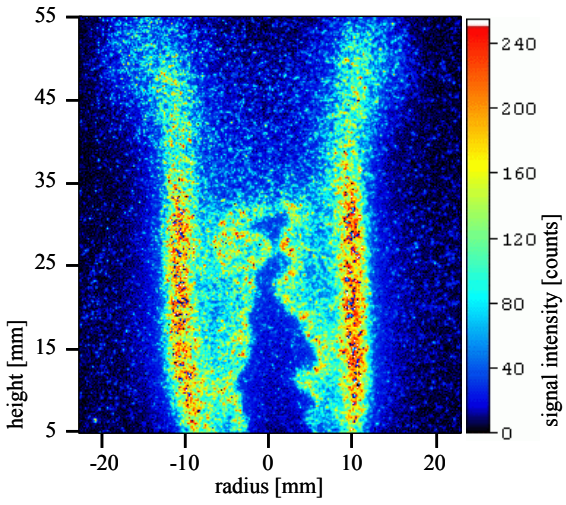

Fig. 1: OH LIF single shot measurement in a flame of a methane/air Bunsen burner, OH excitation by an OPO (Type II) laser system. Excitation frequency at 38,333 cm^{-1}.

With this paper we aim to show the possibilities of OH detection with a tunable OPO (Type II) laser system in flame research. We present investigations of two different atmospheric pressure flames: The flame of a methane/air Bunsen burner and the flame of a hydrogen/oxygen welding torch.
The laser diode pumped Nd:YAG laser system is tunable in the UV wavelength range from 325 nm to 210 nm. Its tuning device consists of an angle tuned Optical Parametric Oscillator (OPO, Type II) and a frequency-

doubling device (SHG, Second Harmonic Generator). The laser output frequency has a bandwidth of about 8 cm^{-1} and a pulse energy of about 5 mJ at 250 nm. With laser light of a specified wavelength, distinct molecules can be excited selectively, for example the OH radical. Our experiments prove, that with the OPO laser system it is possible to change the excitation wavelength within a few seconds. An imaging spectrograph (focal length: 105 mm, aperture ratio: f/4.0, gratings: 1200 grooves/mm and 100 grooves/mm) disperses the scattered light and an intensified CCD camera records the signals.
In order to find appropriate electronic transitions (high signal intensity, no signal superposition of different molecules) to excite the hydroxyl radical for selective laser-induced fluorescence measurements, we scanned the excitation wavelength range from 325 nm to 240 nm (excitation frequency: 30,769 cm^{-1} to 41,667 cm^{-1}). The transitions of the hydroxyl radical $A^2\Sigma^+ \leftarrow X^2\Pi$ (0,0), (1,0), (2,0) and (3,0) bands have been excited and were investigated more intensely.
The paper presents excitation-emission spectra (EES) within the scanned wavelength ranges, the identification of the OH emission peaks and a discussion of the experimental results. The rotational lines of OH, which can be used for selective OH detection are shown. With the high fluorescence signal intensity of the OH A-X (0,0), (1,0) and (2,0) bands, it is possible to get images of 2-dimensional time-resolved qualitative OH distribution. In Fig. 1 a 2-dimensional time-resolved OH LIF measurement of a flame of a methane/air Bunsen burner is shown. The excitation frequency of the OPO (Type II) laser system was set to 38,333 cm^{-1}.
The results of these investigations are aimed at supporting an application of the laser system in a combustion chamber, where industrial burners with a thermal output up to 200 kW can be analyzed.

2. EXPERIMENTAL SETUP and PROCEDURES

2.1 Flames considered

The experiments described in this paper are focused on methane/air and hydrogen/oxygen flames. The methane/air flame is produced using a commercial Bunsen burner, flame diameter ≈30 mm and flame length ≈ 110 mm. The hydrogen/oxygen mixture is burnt with a commercial welding torch, flame diameter ≈ 7 mm and flame length ≈ 200 mm. The hydrogen/oxygen flame of a welding torch offers the advantage of much higher temperature and correspondingly larger OH density. Combustion took place at ambient pressure and air/fuel ratios above 1.

2.2 Experimental setup

Fig. 2 shows a scheme of the experimental setup. A pulsed laser system is used (Infinity-XPO laser, Coherent). The laser diode pumped Nd:YAG laser generates pulses with the fundamental wavelength of 1064 nm. The repetition rate is variable in the range of 0 to 100 Hz. The pulse is amplified by two Nd:YAG rods, the pulse energy accounts up to 500 mJ. After the passage of the pulse through the amplifying system, it is sent through the SHG (Second Harmonic Generation), an angle tuned BBO crystal (Beta Barium Borate). In the crystal, the infrared radiation undergoes doubling. The two beams of 1064 nm and 532 nm are sent through a second angle tuned BBO crystal (THG, Third Harmonic Generation) where they undergo a frequency mixing. The radiation produced at 354.7 nm is thereafter separated from the infrared and doubled radiation. The pulse energy rates up to 160 mJ.
In a tunable Optical Parametric Oscillator (OPO, Type II), light at 354.7 nm is injected in a crystal, which provides light of two other wavelengths, the "signal" and the "idler". In the experiments, only the signal wavelength is used. The signal wavelength is tunable from 709.4 nm to 420 nm, dependent on the angle position of the crystal. Behind of the OPO, the SHG arrangement allows doubling of the OPO signal wavelength. Therefore, in the UV-range the pulsed laser system is tunable from 325 nm down to 210 nm. At wavelengths from 325 nm to 210 nm the maximum UV laser energy of a single pulse is about 5 mJ. The pulse duration is 3 ns in average and the laser bandwidth of a single shot measures about 8 cm^{-1}. The laser light is linearly polarized with its E-vector lying in the vertical plane, i.e. perpendicular with the detection axis.
The laser beam is focused by a convex cylindrical lens. Behind the first burner (methane/air Bunsen burner or hydrogen/oxygen welding torch) a second cylindrical convex lens transforms the UV laser beam to a laser sheet of 60 mm height and 0,5 mm width. This laser sheet crosses the second burner, a methane/air Bunsen burner or hydrogen/oxygen burner (in some experiments also symmetric-convex lenses are used).
Two intensified CCD cameras (ICCD) were used for detection (FlameStar, LaVision). The cameras include an UV-sensitive gateable microchannel plate image intensifier (I/I) and a slow scan CCD sensor. The ICCD camera 1 delivers information about wavelength and position of excited molecules using an UV-light permeable objective, focal length 105 mm and f/4.5 aperture (UV Nikkor, Nikon) and an imaging spectrograph (250IS, CHROMEX). The spectrograph is a 250-mm-focal-length, f/4.0 aperture ratio model equipped with three different gratings. In these tests the gratings with 1200 grooves/mm, blaze wavelength 200 nm and 100 grooves/mm, blaze wavelength 450 nm were used. The spectrograph is mounted with the entrance slit (50 μm) oriented paral-

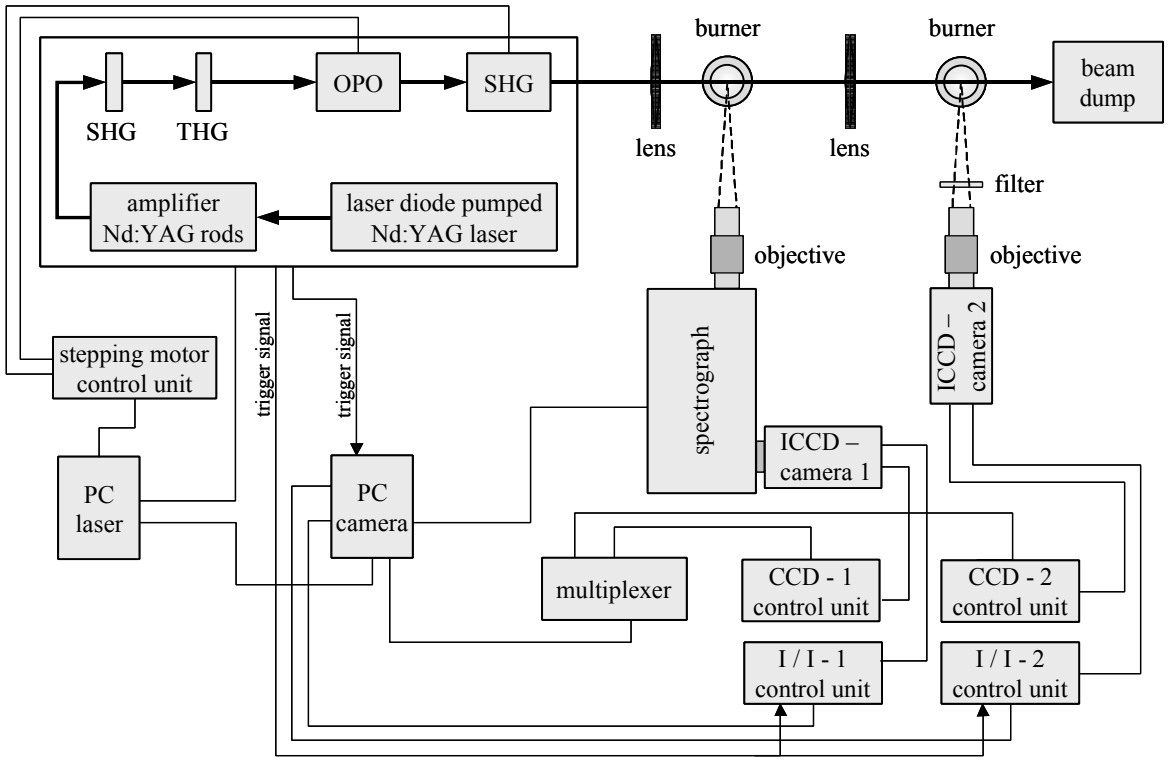

Fig. 2: Experimental setup for spectrally resolved or time-resolved laser-induced fluorescence (LIF) measurements in different flames.

lel to the laser beam's propagation direction . The spectral system response was calibrated using a mercury argon lamp.

The second ICCD camera permits spatial-resolved and time-resolved 2D-images of the flames. Rayleigh scattering light was separated from LIF signal with UV transmitting black glass filters (UG11 and UG5, Melles Griot). The two CCD control units and two I/I control units are controlled by a personal computer (PC camera). With a second computer (PC laser), the laser system is managed and the crystals in the OPO and SHG are turned via a stepping motor control unit in order to vary laser output wavelength. The laser system provides a trigger signal for the camera system and the image intensifier (I/I units).

2.3 Experimental procedure

To record the excitation-emission spectra (EES), the laser beam is focused two centimetres outside the flame front/reaction zone in order to avoid two-photon photo dissociation of H_2O (Frodermann, 1996). The measurements in the methane/air flame are carried out in the reaction zone, 20 mm above the mouth of the Bunsen burner. In the hydrogen/oxygen flame, investigation took place in the reaction zone 50 mm above the outlet of the welding torch.

For each line of the EES shown in chapter 3.1, 50 laser pulses were summed up and signal intensities of the reaction zone were averaged. The laser wavelength was tuned in 0.0125 nm steps. In the measurements presented in chapters 3.2, 3.3 and 3.4, 60 laser pulses were summed up. Signal intensities of the reaction zone were averaged and the laser wavelength was tuned in 0.01 nm steps.

3. MEASUREMENTS, RESULTS and DISCUSSION

Four excitation wavelength ranges are studied thoroughly.

Chapter 3.1: OH A-X (0,0), (1,1) and (2,2) bands from 321.0 nm to 302.0 nm (31,153 cm^{-1} to 33,113 cm^{-1}).
Chapter 3.2: OH A-X (1,0) and (2,1) bands from 291.0 nm to 278.5 nm (34,364 cm^{-1} to 35,907 cm^{-1}).
Chapter 3.3: OH A-X (2,0) and (3,1) bands from 271.0 nm to 259.0 nm (36,900 cm^{-1} to 38,610 cm^{-1}).
Chapter 3.4: OH A-X (3,0) and (4,1) bands from 251.1 nm to 242.1 nm (39,825 cm^{-1} to 41,305 cm^{-1}).

3.1 OH excitation within the A-X (0,0), (1,1) and (2,2) bands

The flame of a methane/air Bunsen burner is investigated in the excitation wavelength range from 321.0 nm to 302.0 nm (31,153 cm^{-1} to 33,113 cm^{-1}). The laser beam is focused with a symmetric-convex lens (Suprasil 1, Heraeus), focal length 300 mm. The focus of the laser beam is about 4 centimetres outside the region investigated. Fluorescence and Rayleigh signals are averaged in the flame front/reaction zone of the Bunsen burner.

In Fig. 3 an excitation-emission spectrum (EES) of a methane/air flame is shown. The excitation wavelength is tuned from 321.0 nm down to 302.0 nm. The emission wavelength is detected from 300 nm to 327 nm. The EES is recorded with the 1200 grooves/mm grating. In the excitation-emission spectrum of Fig. 3 signals of Rayleigh scattering and laser-induced fluorescence are shown. The line of the elastic Rayleigh scattering signal starts at an emission wavelength of 321.0 nm at the upper side of the figure and ends at an emission wavelength of 302 nm at the bottom respectively to the excitation wavelength of the laser. In order to reduce the signal intensity of Rayleigh scattering, the laser's E-vector was turned 90° into the horizontal plane by a polarization rotator. Signals of Rayleigh scattering interfere with fluorescence signals. The signals in the excitation-emission spectrum have been identified as laser-induced fluorescence of hydroxyl radicals. In the tuned excitation range electronic transitions of hydroxyl are $A^2\Sigma^+$ (v' = 0) ← $X^2\Pi$ (v'' = 0), $A^2\Sigma^+$ (v' = 1) ← $X^2\Pi$ (v'' = 1) and $A^2\Sigma^+$ (v' = 2) ← $X^2\Pi$ (v'' = 2) (Herzberg, 1971). The excitation of OH in the (0,0) band starts at a calculated excitation frequency of 33,088.6 cm^{-1}. Rotational lines of the OH radical are found in the whole range. Transitions in the (1,1) band start at a calculated excitation frequency of 32,423.8 cm^{-1} and at an excitation frequency of 31,733.8 cm^{-1} the transitions in the (2,2) band start. In comparison to the rotational lines of the (0,0) band, transitions in the (1,1) and (2,2) bands have a low intensity.

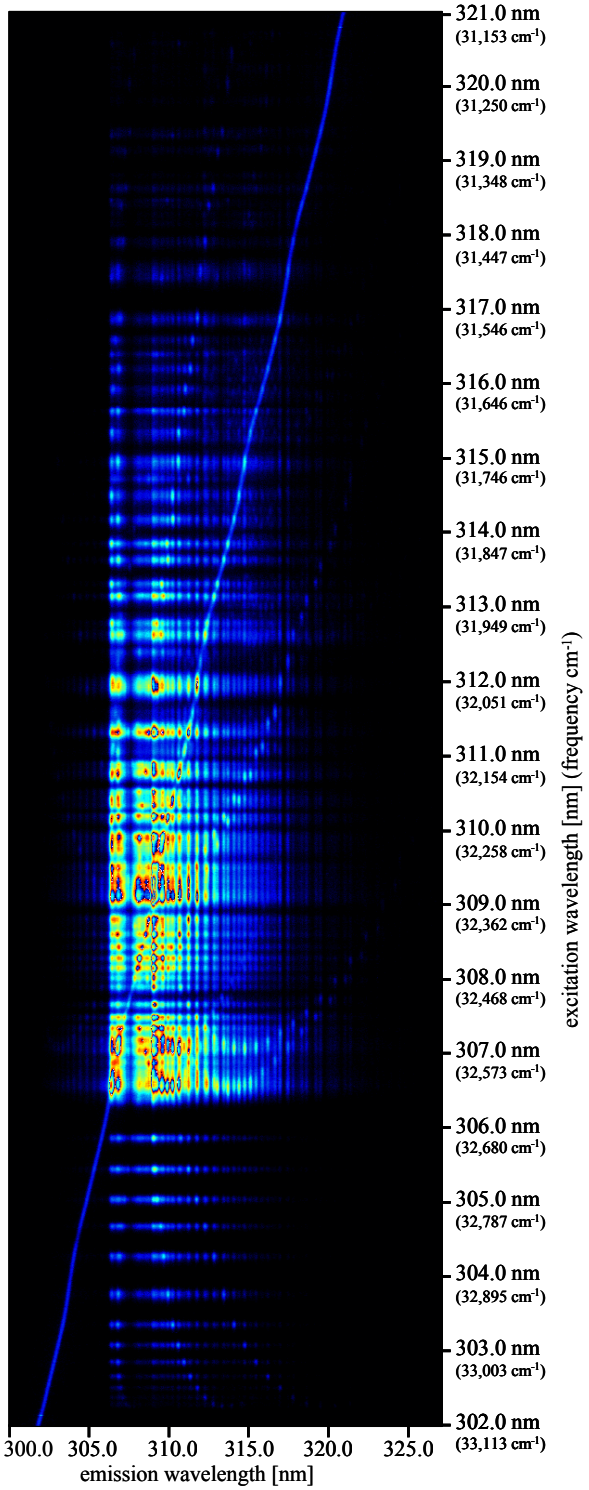

Fig. 3: Excitation-emission spectrum of a methane/air Bunsen burner flame. The excitation wavelength is tuned from 321 nm to 302 nm. The emissions are detected from 300 nm to 327 nm.

In the middle part of Fig. 3 (emission wavelength from about 305 nm to 320 nm) superposition of Rayleigh scattering (slope) and OH fluorescence occurs. The OH emissions are within the (0 → 0), (1 → 1) and (2 → 2) bands (Vibrational energy transfer, VET).

In search of the most intensive transitions of the hydroxyl radical in order to visualize OH distribution in different flames the rotational lines of the $A^2\Sigma^+$ ← $X^2\Pi$ (0,0), (1,1) and (2,2) transitions are identified with the computer program LIFBASE (Luque and Crosley, 1999).

Fig. 4 displays an excitation spectrum of OH in a methane/air flame within the excitation wavelength range from 321.0 nm to 302.0 nm. Fluorescence signals are averaged in the emission wavelength interval from 306.2 nm to 307.2 nm. Because of the bandwidth of the laser (≈ 8 cm^{-1} at 305 nm), the discrete OH peaks result from excitation of several rotational lines at the same time. In most cases it is not possible, to excite single rotational lines of the OH A-X (0,0), (1,1) or (2,2) bands. Table 1 shows the identification of the rotational lines of the peaks, labeled in Fig. 4. For all peaks applies: The upper right corner shows the measured maximum intensity of the peak in [cm^{-1}]. All calculated rotational lines are given in [cm^{-1}]. Rotational lines with high intensity, e.g. at least 50 percent of the most intense line of this peak, are printed in bold face and with a grey background. The lines with an intensity between 50 and 10 percent of the most intense line of this peak, are printed in bold face. Rotational lines with an intensity between 10 and 2 percent of the most intense line of this peak, are printed italic. Finally, rotational lines with an intensity of less than 2 percent are not shown. For the calculation the rotational temperature T_{rot} and vibrational temperature T_{vib} amount to 2000 K.

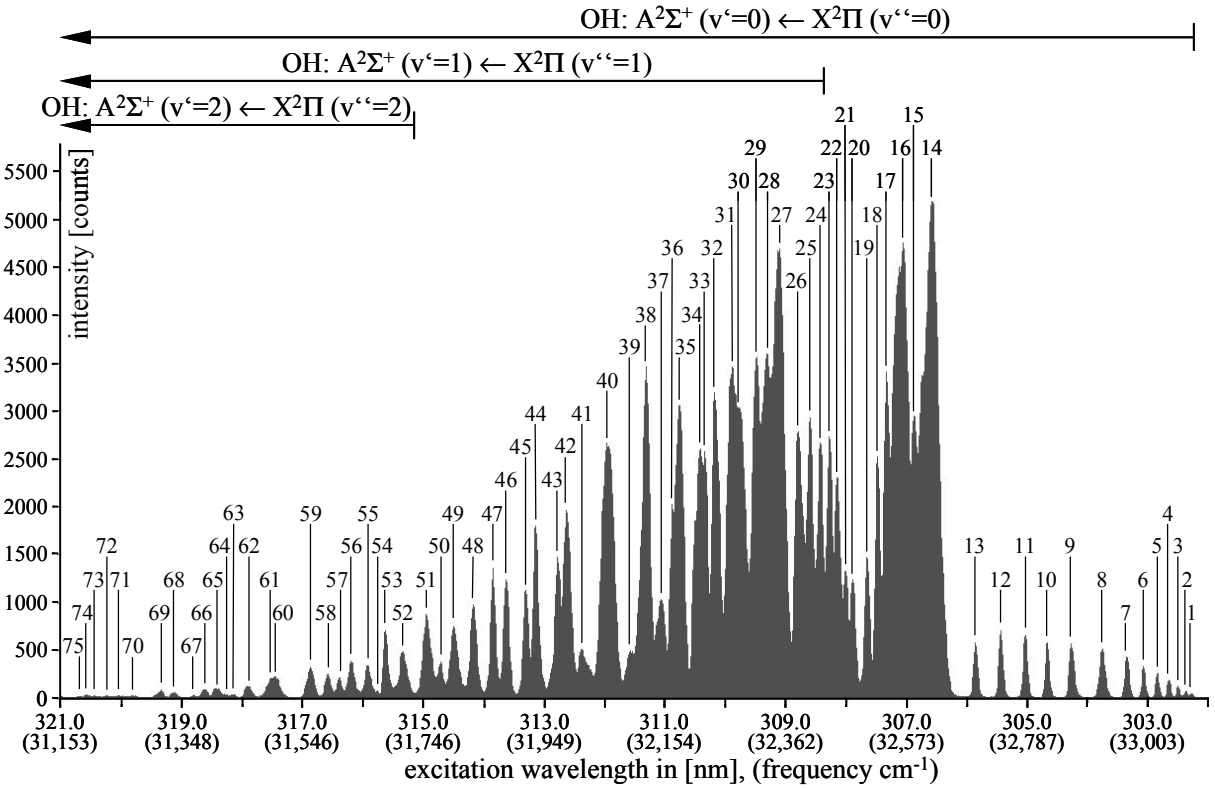

Fig. 4: Excitation spectrum of hydroxyl in a methane/air flame. The excitation wavelength ranges from 321.0 nm to 302.0 nm. Fluorescence signals are averaged in the emission wavelength interval from 306.2 nm to 307.2 nm. The rotational lines of labeled peaks are shown in Table 1.

To record 2-dimensional spatial-resolved OH distribution it is necessary to separate OH LIF from Rayleigh scattering with adequate filters. Fig. 3 shows superposition of Rayleigh scattering signals and OH fluorescence signals in the $(0 \rightarrow 0)$, $(1 \rightarrow 1)$ and $(2 \rightarrow 2)$ bands. However the high intensities of the emissions (especially by excitation at peaks 15, 16 or 27, of Fig. 4), allow measurements of qualitative OH distribution in flames, without separating Rayleigh scattering from LIF.

Peak 1	33,081
$S_{21}(15)$	33,088.6
$S_{21}(14)$	33,083.7
$S_{21}(17)$	33,083.3

Peak 2	33,072
$S_{21}(13)$	33,073.8
$S_{21}(18)$	33,072.6

Peak 3	33,056
$S_{21}(12)$	33,059.1
S_{21} (19)	*33,056.3*

Peak 4	33,040
$S_{21}(11)$	33,039.9
S_{21} (20)	*33,034.3*

Peak 5	33,020
$S_{21}(10)$	33,016.2

Peak 6	32,994
$S_{21}(9)$	32,988.3

Peak 7	32,964
$S_{21}(8)$	32,956.3

Peak 8	32,920
$S_{21}(7)$	32,920.5

Peak 9	32,864
$S_{21}(6)$	32,881.1

Peak 10	32,822
$S_{21}(5)$	32,838.4

Peak 11	32,783
$S_{21}(4)$	32,792.8

Peak 12	32,739
$S_{21}(3)$	32,744.6

Peak 13	32,694
$S_{21}(2)$	32,694.6

Peak 14	32,617
S_{21} (1)	*32,643.4*
$R_1(9)$	32,632.2
$R_1(8)$	32,630.5
$R_1(10)$	32,630.5
R_{21} (9)	*32,629.9*
$R_{21}(8)$	32,628.4
R_{21} (10)	*32,627.9*
$R_1(7)$	32,625.6
$R_1(11)$	32,625.1
$R_{21}(7)$	32,623.6
R_{21} (11)	*32,622.3*
$R_1(6)$	32,617.5
$R_1(12)$	32,616.0
$R_{21}(6)$	32,615.8
R_{21} (12)	*32,612.9*

Peak 15	32,585
$R_1(5)$	32,606.6
$R_{21}(5)$	32,605.1
$R_1(13)$	32,603.0

Peak 16	32,567
R_{21} (13)	*32,599.7*
$R_1(4)$	32,593.1
$R_{21}(4)$	32,591.9
$R_2(10)$	32,588.6
$R_2(9)$	32,587.4
$R_1(14)$	32,585.9
$R_2(11)$	32,585.6
$R_2(8)$	32,582.0
$R_2(12)$	32,578.5
$R_1(3)$	32,577.6
$R_{21}(3)$	32,576.6
$R_2(7)$	32,572.5

Peak 17	32,538
$R_2(13)$	32,567.1
$R_1(15)$	32,564.8
$R_1(2)$	32,560.5
$R_{21}(2)$	32,559.7
$R_2(6)$	32,558.7
$R_2(14)$	32,551.5

Peak 18	32,522
$R_1(1)$	32,542.5
$R_{21}(1)$	32,542.0
$R_2(5)$	32,540.5
$R_1(16)$	32,539.4
$R_2(15)$	32,531.5

Peak 19	32,503
$R_2(4)$	32,517.5
$R_1(17)$	32,509.6
$R_2(16)$	32,507.0

Peak 20	32,478
$R_2(3)$	32,489.5

Peak 21	32,466
$R_2(17)$	32,478.1
R_1 (18)	*32,475.3*
$Q_1(1)$	32,474.6
$Q_{21}(1)$	32,474.2

Peak 22	32,452
$Q_1(2)$	32,458.6
$Q_{21}(2)$	32,458.0
$R_2(2)$	32,455.7

Peak 23	32,437
R_2 (18)	*32,444.5*
$Q_1(3)$	32,441.8
$Q_{21}(3)$	32,441.0
$P_1(1)$	32,440.6
R_1 (19)	*32,436.4*

Peak 24	32,421
$Q_1(4)$	32,423.6
$Q_{21}(4)$	32,422.6
$R_2(1)$	32,415.5

Peak 25	32,404
$Q_1(5)$	32,403.4
$Q_{21}(5)$	32,402.2

*) rotational lines of the OH A-X (1,1) band

**) rotational lines of the OH A-X (2,2) band

Table 1, part I: OH A-X (0,0), (1,1) and (2,2) transitions. Identification of the rotational lines of the peaks, labeled in Fig. 4. The excitation frequencies are in [cm^{-1}]. In the upper right corner: measured excitation frequency of the peak . The rotational lines are shown with the calculated excitation frequencies.

Peak 26	32,383
$P_1(2)$	32,390.9
$Q_1(6)$	32,380.9
$Q_{21}(6)$	32,379.4

Peak 27	32,349
$Q_1(7)$	32,355.8
$Q_{12}(3)$	32,355.4
$Q_{12}(2)$	32,355.0
$Q_2(3)$	32,354.6
$Q_2(2)$	32,354.5
$Q_{21}(7)$	32,354.1
$Q_{12}(4)$	32,350.2
$Q_2(4)$	32,349.2
$Q_{12}(1)$	32,348.3
$Q_2(1)$	32,348.0

Peak 28	32,328
$P_1(3)$	32,340.6
$Q_{12}(5)$	32,340.0
$Q_2(5)$	32,338.8

Peak 29	32,312
$Q_1(8)$	32,328.0
$Q_{21}(8)$	32,326.1
$Q_{12}(6)$	32,325.3
$Q_2(6)$	32,323.9
$P_{12}(1)$	32,314.1

Peak 30	32,281
$Q_{12}(7)$	32,306.5
$Q_2(7)$	32,304.8
$Q_1(9)$	32,297.2
$Q_{21}(9)$	32,295.1

Peak 31	32,268
$P_1(4)$	32,289.1
$P_{12}(2)$	32,286.9
$P_2(2)$	32,286.5
$Q_{12}(8)$	32,283.6
$Q_2(8)$	32,281.7

Peak 32	32,239
$Q_1(10)$	32,263.4
$Q_{21}(10)$	32,261.0
$Q_{12}(9)$	32,256.9
$Q_2(9)$	32,254.8
$P_{12}(3)$	32,253.5
$O_{12}(2)$	32,253.1
$P_2(3)$	32,252.9

Peak 33	32,222
$P_1(5)$	32,235.9

Peak 34	32,214
$Q_{12}(10)$	32,226.5
$Q_1(11)$	32,226.4
$Q_2(10)$	32,224.1
$Q_{21}(11)$	32,223.8
$P_{12}(4)$	32,214.7
$P_2(4)$	32,214.0

Peak 35	32,178
$Q_{12}(11)$	32,192.4
$Q_2(11)$	32,189.8
$Q_1(12)$	32,186.2
$O_{12}(3)$	32,185.8
$Q_{21}(12)$	32,183.4
$P_1(6)$	32,180.8

Peak 36	32,166
$P_{12}(5)$	32,171.3
$P_2(5)$	32,170.3

Peak 37	32,148
$Q_{12}(12)$	32,154.7
$Q_2(12)$	32,151.8
$Q_1(13)$	32,142.7
$Q_{21}(13)$	32,139.6

Peak 38	32,121
$P_{12}(6)$	32,123.7
$P_1(7)$	32,123.4
$P_2(6)$	32,122.5
$O_{12}(4)$	32,113.2
$Q_2(13)$	32,110.2

Peak 39	32,094
$Q_1(14)$	32,095.7
$Q_{21}(14)$	32,092.5

Peak 40	32,056
$P_{12}(7)$	32,072.3
$P_2(7)$	32,070.8
$Q_2(14)$	32,064.9
$P_1(8)$	32,063.7

Peak 41	32,011
$Q_1(15)$	32,045.3
$Q_{21}(15)$	32,041.8
$O_{12}(5)$	32,036.0

Peak 42	31,986
$R_1(8)$*	32,025.1
$R_1(7)$*	32,023.8
$R_1(9)$*	32,022.7
$R_1(6)$*	32,019.2
$P_{12}(8)$	32,017.3
$R_1(10)$*	32,016.7
$Q_2(15)$	32,015.9
$P_2(8)$	32,015.6
$R_1(5)$*	32,011.6
$R_{21}(5)$*	32,010.2

Peak 43	31,971
$R_1(11)$*	32,006.7
$P_1(9)$	32,001.5
$R_1(4)$*	32,001.1
$R_{21}(4)$*	31,999.9
$R_1(12)$*	31,992.7
$Q_1(16)$	31,991.4
$R_1(3)$*	31,988.2
$R_{21}(3)$*	31,987.3

Peak 44	31,934
$R_2(9)$*	31,977.0
$R_2(8)$*	31,975.6
$R_1(13)$*	31,974.5
$R_2(10)$*	31,974.0
$R_1(2)$*	31,973.5
$R_{21}(2)$*	31,972.8
$R_2(7)$*	31,969.8
$R_2(11)$*	31,966.5
$Q_2(16)$	31,963.1
$R_2(6)$*	31,959.4
$P_{12}(9)$	31,959.0
$P_2(9)$	31,957.1
$R_{21}(1)$*	31,957.1
$O_{12}(6)$	31,954.7
$R_2(12)$*	31,954.6

Peak 45	31,917
$R_2(5)$*	31,944.3
$R_2(13)$*	31,938.1
$P_1(11)$	31,936.8
$Q_1(17)$	31,933.8
$R_2(4)$*	31,924.3

Peak 46	31,884
$Q_2(17)$	31,906.5
$R_2(3)$*	31,898.9
$P_{12}(10)$	31,897.5
$P_2(10)$	31,895.3
$Q_1(1)$*	31,893.0
$Q_{21}(1)$*	31,892.7

Peak 47	31,861
$Q_1(2)$*	31,876.7
$Q_{21}(2)$*	31,876.1
$Q_1(18)$	31,872.4
$O_{12}(7)$	31,869.7
$P_1(11)$	31,869.4
$R_2(2)$*	31,867.7
$P_1(1)$*	31,860.7
$Q_1(3)$*	31,859.2
$Q_{21}(3)$*	31,858.5

Peak 48	31,828
$Q_2(18)$	31,846.1
$Q_1(4)$*	31,840.0
$Q_{21}(4)$*	31,839.0
$P_{12}(11)$	31,832.8
$P_2(11)$	31,830.4
$R_2(1)$*	31,830.0
$Q_1(5)$*	31,818.5
$Q_{21}(5)$*	31,817.3

Peak 49	31,795
$P_1(2)$*	31,812.3
$Q_1(19)$	31,807.3
$P_1(12)$	31,799.4
$Q_1(6)$*	31,794.5
$Q_{21}(6)$*	31,793.1

Peak 50	31,774
$Q_2(19)$	31,781.8
$O_{12}(8)$	31,781.5

Peak 51	31,750
$Q_{12}(2)$*	31,772.0
$Q_{12}(3)$*	31,771.5
$Q_2(2)$*	31,771.5
$Q_2(3)$*	31,770.8
$Q_1(7)$*	31,767.6
$Q_{12}(1)$*	31,766.2
$Q_{21}(7)$*	31,766.0
$Q_2(1)$*	31,765.8
$Q_{12}(4)$*	31,765.3
$P_{12}(12)$	31,765.0
$Q_2(4)$*	31,764.3
$P_1(3)$*	31,763.0
$P_2(12)$	31,762.4
$Q_{12}(5)$*	31,753.8
$Q_2(5)$*	31,752.6

Peak 52	31,711
$Q_1(20)$	31,738.3
$Q_1(8)$*	31,737.7
$Q_{12}(6)$*	31,737.6
$Q_2(6)$*	31,736.2
$Q_{21}(8)$*	31,735.8
$P_{12}(1)$*	31,733.6
$P_1(13)$	31,726.8
$Q_{12}(7)$*	31,717.0
$Q_2(7)$*	31,715.4
$Q_2(20)$	31,713.5
$P_1(4)$*	31,712.1

Peak 53	31,682
$P_{12}(2)$*	31,707.2
$P_2(2)$*	31,706.9
$Q_1(9)$*	31,704.6
$P_{12}(13)$	31,694.2
$P_2(13)$	31,691.4
$Q_2(8)$*	31,690.3
$O_{12}(9)$	31,690.1

Peak 54	31,668
$O_{12}(2)$*	31,675.1
$P_{12}(3)$*	31,674.6
$P_2(3)$*	31,674.1
$Q_1(10)$*	31,668.1
$Q_{21}(10)$*	31,665.9
$Q_1(21)$	31,665.3
$Q_{12}(9)$*	31,663.2
$Q_2(9)$*	31,661.2

Peak 55	31,652
$P_1(5)$*	31,659.3
$P_1(14)$	31,651.3
$Q_2(21)$	31,641.1
$P_{12}(4)$*	31,636.5
$P_2(4)$*	31,635.7

Peak 56	31,624
$Q_1(11)$*	31,628.3
$Q_2(10)$*	31,628.0
$P_{12}(14)$	31,620.4
$P_2(14)$	31,617.3
$O_{12}(3)$*	31,610.3

Peak 57	31,606
$P_1(6)$*	31,604.2
$O_{12}(10)$	31,595.8
$P_{12}(5)$*	31,593.4
$P_2(5)$*	31,592.5
$Q_2(11)$*	31,590.9
$Q_1(22)$	31,588.1
$Q_1(12)$*	31,584.9
$Q_{21}(12)$*	31,582.2

Peak 58	31,587
$P_1(15)$	31,573.1
$Q_2(22)$	31,564.5

Peak 59	31,557
$Q_2(12)$*	31,549.8
$P_1(7)$*	31,546.7
$P_{12}(6)$*	31,546.0
$P_2(6)$*	31,544.8
$P_{12}(15)$	31,543.6
$P_2(15)$	31,540.3
$O_{12}(4)$*	31,540.0
$Q_1(13)$*	31,537.9

Peak 60	31,500
$Q_1(23)$	31,506.8
$Q_2(13)$*	31,504.7
$O_{12}(11)$	31,498.7
$P_{12}(7)$*	31,494.5
$P_2(7)$*	31,493.1
$P_1(16)$	31,492.1

Peak 61	31,494
$Q_1(14)$*	31,487.2
$P_1(8)$*	31,486.5
$Q_2(23)$	31,483.6

Peak 62	31,455
$O_{12}(5)$*	31,464.8
$P_{12}(16)$	31,463.7
$P_2(16)$	31,460.2
$Q_2(14)$*	31,455.7

Peak 63	31,430
$P_{12}(8)$*	31,439.2
$P_2(8)$*	31,437.5
$Q_1(15)$*	31,432.7

Peak 64	31,417
$P_1(9)$*	31,423.6
$Q_1(24)$	31,421.1

Peak 65	31,403
$P_1(17)$	31,408.2
$Q_2(15)$*	31,402.6
$O_{12}(12)$	31,399.0
$Q_2(24)$	31,398.3

Peak 66	31,384
$O_{12}(6)$*	31,385.4
$P_{12}(17)$	31,380.9
$P_{12}(9)$*	31,380.2
$P_2(9)$*	31,378.4
$P_2(17)$	31,377.2
$Q_1(16)$*	31,374.3

Peak 67	31,366
$P_1(11)$*	31,357.9
$Q_2(16)$*	31,345.5

Peak 68	31,333
$Q_1(25)$	31,330.9
$P_1(18)$	31,321.4
$P_{12}(10)$*	31,317.7
$P_2(10)$*	31,315.7
$Q_1(17)$*	31,312.0

Peak 69	31,312
$Q_2(25)$	31,308.5
$O_{12}(7)$*	31,302.0
$O_{12}(13)$	31,296.7
$P_{12}(18)$	31,295.0
$P_2(18)$	31,291.0
$P_1(11)$*	31,289.3
$Q_2(17)$*	31,284.2

Peak 70	31,268
$P_{12}(11)$*	31,251.9
$P_2(11)$*	31,249.6
$R_{21}(15)$**	31,246.7
$Q_1(18)$*	31,245.5

Peak 71	31,244
$P_1(19)$	31,231.7

Peak 72	31,226
$Q_2(18)$*	31,218.7
$P_1(12)$*	31,217.8
$O_{12}(8)$*	31,215.0
$Q_2(26)$	31,214.1

Peak 73	31,206
$P_{12}(19)$	31,206.0
$P_2(19)$	31,201.8

Peak 74	31,193
$O_{12}(14)$	31,192.0

Peak 75	31,179
$P_{12}(12)$*	31,182.6
$P_2(12)$*	31,180.1
$Q_1(6)$**	31,177.5

*) rotational lines of the OH A-X (1,1) band **) rotational lines of the OH A-X (2,2) band

Table 1, part II: OH A-X (0,0), (1,1) and (2,2) transitions. Identification of the rotational lines of the peaks, labeled in Fig. 4. The excitation frequencies are in [cm^{-1}]. In the upper right corner: measured excitation frequency of the peak. The rotational lines are shown with the calculated excitation frequencies.

3.2 OH excitation within the A-X (1,0) and (2,1) bands

The flame of a methane/air Bunsen burner is investigated in the excitation wavelength range from 291.0 nm to 278.5 nm (34,364 cm^{-1} to 35,907 cm^{-1}). The laser beam is focused with a symmetric-convex lens (Suprasil 1, Heraeus), focal length 150 mm. The focus of the laser beam is about two centimetres outside the region investigated. Fluorescence and Rayleigh signals are averaged in the flame front/reaction zone of the Bunsen burner.
Fig. 5 shows an excitation-emission spectrum of a methane/air flame. The excitation wavelength is tuned from 291.0 nm down to 278.5 nm. For each line we summed up 60 laser pulses and averaged the signal intensities of the reaction zone. The laser wavelength is tuned in 0.01 nm steps. The figure displays emission wavelength from 275.0 nm to 327.0 nm. The EES is recorded with the 1200 grooves/mm grating. Outside the emission wavelength range displayed in Fig. 5 no further fluorescence signals could be observed.

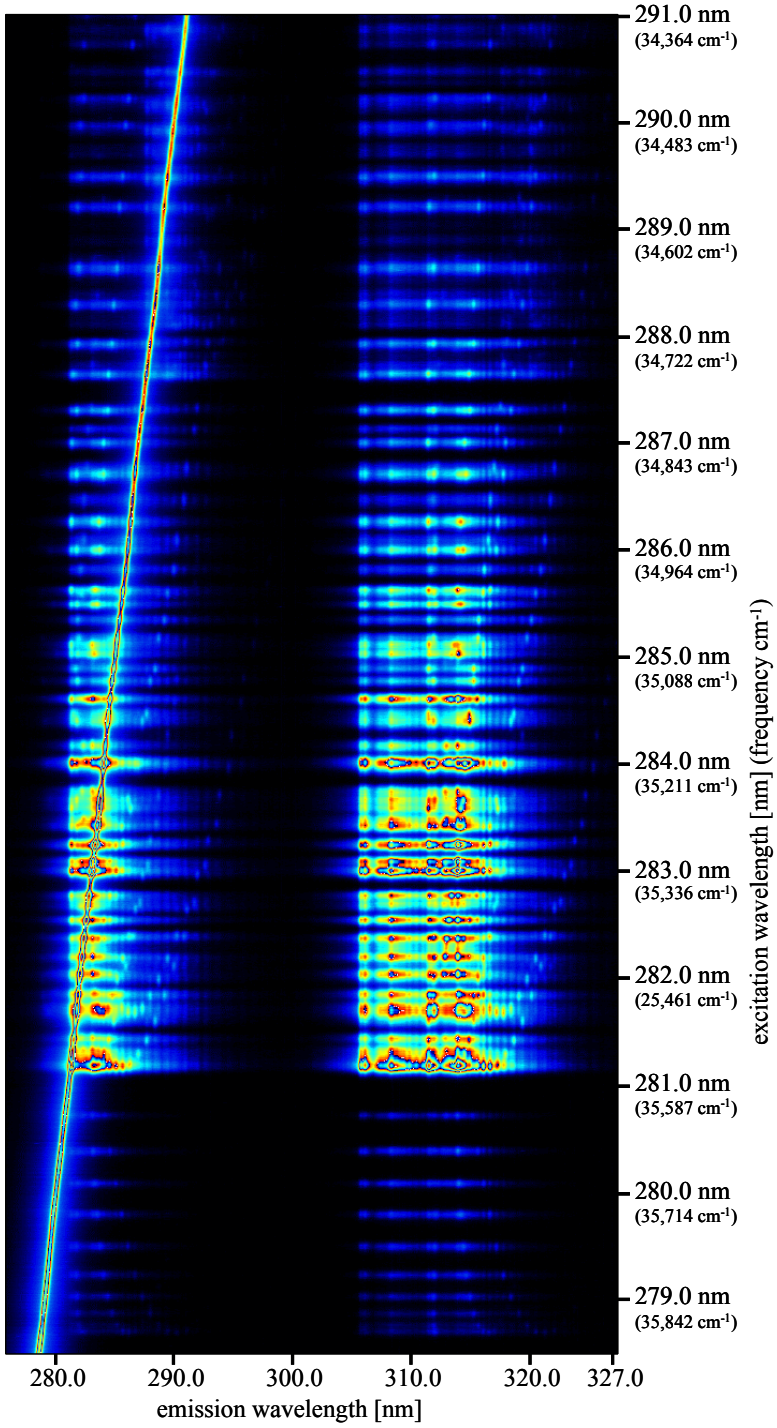

Fig. 5: Excitation-emission spectrum of a methane/air Bunsen burner flame. The excitation wavelength is tuned from 291.0 nm to 278.5 nm. The emissions are detected from 275 nm to 327 nm.

The signals in the excitation-emission spectrum (EES) have been identified as laser-induced fluorescence of hydroxyl radicals. In the tuned excitation range electronic transitions of OH are $A^2\Sigma^+ (v' = 1) \leftarrow X^2\Pi (v'' = 0)$ and $A^2\Sigma^+ (v' = 2) \leftarrow X^2\Pi (v'' = 1)$ (Herzberg, 1971). The excitation of OH in the (1,0) band starts at a calculated excitation frequency of 35,876.9 cm^{-1}, rotational lines are found in the entire range. Transitions in the (2,1) band start at a calculated excitation frequency of 35,044.3 cm^{-1} (Luque and Crosley, 1999). In comparison to the rotational lines of the (1,0) band, transitions in the (2,1) band have a low intensity.
In the left part of Fig. 5 superposition of Rayleigh scattering (slope) and OH fluorescence within the $(1 \rightarrow 0)$ and $(2 \rightarrow 1)$ bands occurs. Beginning with an emission wavelength of about 305 nm OH fluorescence in the $(0 \rightarrow 0)$, $(1 \rightarrow 1)$ and $(2 \rightarrow 2)$ bands are found in the right section of the EES.
In search of the most intensive transitions of the hydroxyl radical in order to visualize OH distribution in different flames the rotational lines of the $A^2\Sigma^+ \leftarrow X^2\Pi$ (1,0) and (2,1) transitions are identified with the computer program LIFBASE (Luque and Crosley, 1999).
Fig. 6 displays the excitation spectrum of OH in a methane/air flame within the excitation wavelength range from 291.0 nm to 278.5 nm. Fluorescence signals are averaged in the emission wavelength interval from 305 nm to 317 nm, $(0 \rightarrow 0)$, $(1 \rightarrow 1)$ and $(2 \rightarrow 2)$ bands.
Table 2 shows the identification of the rotational lines of the peaks, labeled in

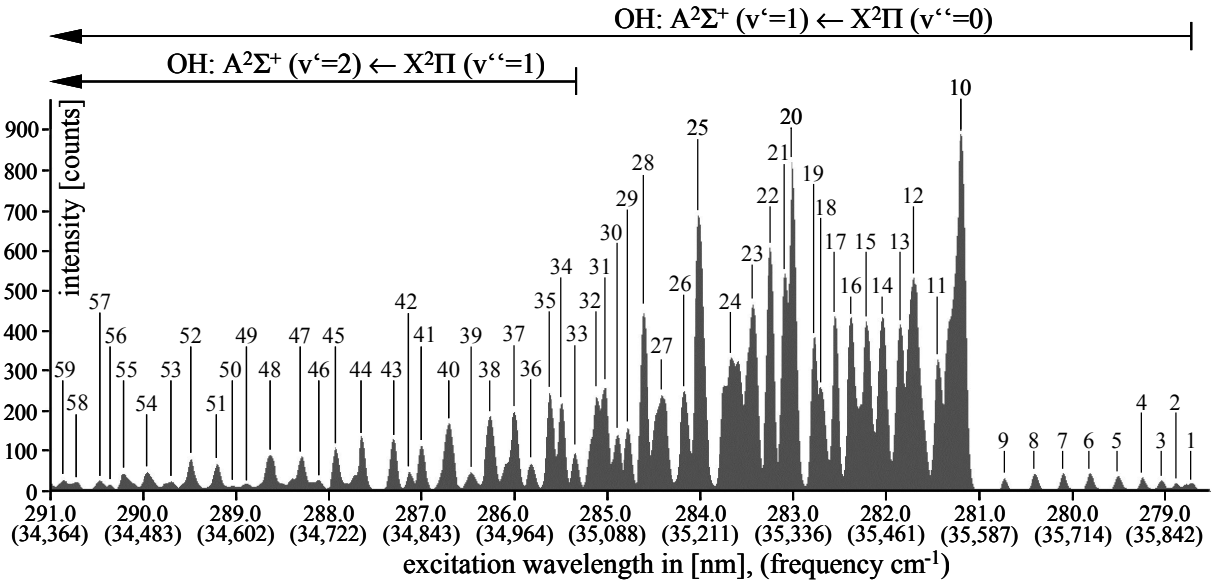

Fig. 6:Excitation spectrum of hydroxyl in a methane/air flame. The excitation wavelength ranges from 291.0 nm to 278.5 nm. The fluorescence signals are averaged in the emission wavelength interval from 305.0 nm to 317.0 nm. The rotational lines of labeled peaks are shown in Table 2.

Fig. 6. In most cases it is not possible, to excite single rotational lines of the OH A-X (1,0) or (2,1) transition, because of the bandwidth of the laser of about 8 cm^{-1} at 287 nm. As a consequence the peaks in Fig. 6 display simultaneous excitation of several rotational lines of the hydroxyl radical.

For all peaks in Table 2 applies: The upper right corner shows the measured maximum intensity of the peak in [cm^{-1}]. All calculated rotational lines are given in [cm^{-1}]. Rotational lines with high intensity, e.g. at least 50 percent of the most intense line of this peak, are printed in bold face and with a grey background. The lines with an intensity between 50 and 10 percent of the most intense line of this peak, are printed in bold face. Rotational lines with an intensity between 10 and 2 percent of the most intense line of this peak, are printed italic. Finally, rotational lines with an intensity of less than 2 percent are not shown. For the calculation the rotational temperature T_{rot} is 1600 K and the vibrational temperature T_{vib} amounts to 2200 K.

The excitation spectrum presented in Fig. 6 shows that, because of their high signal intensity, peaks labeled 10, 12, 20, 22 and 25 are especially suited to detect OH and to image an qualitative OH distribution.

To record 2-dimensional spatial-resolved OH distribution it is necessary to separate OH LIF from Rayleigh scattering with adequate filters. Because of superposition of Rayleigh scattering signals and OH fluorescence signals in the ($1 \rightarrow 0$) and ($2 \rightarrow 1$) bands, the signals of this bands can not be used for spatial OH detection. However the high intensity of the emission in the ($0 \rightarrow 0$), ($1 \rightarrow 1$) and ($2 \rightarrow 2$) bands (emission wavelength from about 305 nm to 325 nm) allow to measure distribution of hydroxyl radicals in flames.

Peak 1	35,878
$S_{21}(11)$	35,876.9
$S_{21}(10)$	35,874.8
$S_{21}(12)$	35,872.9
$S_{21}(9)$	35,866.9
$S_{21}(13)$	35,862.6

Peak 2	35,858
$S_{21}(8)$	35,853.2
$S_{21}(14)$	35,845.9

Peak 3	35,837
$S_{21}(7)$	35,834.1
$S_{21}(15)$	35,822.7

Peak 4	35,811
$S_{21}(6)$	35,809.7

Peak 5	35,777
$S_{21}(5)$	35,780.3

Peak 6	35,739
$S_{21}(4)$	35,746.3

Peak 7	35,702
$S_{21}(3)$	35,708.2

Peak 8	35,663
$S_{21}(2)$	35,666.5

Peak 9	35,621
$S_{21}(1)$	35,621.9

Peak 10	35,562
$R_1(5)$	35,560.0
$R_1(6)$	35,559.3
$R_{21}(5)$	35,558.6
$R_{21}(6)$	35,557.6
$R_1(4)$	35,556.6
$R_{21}(4)$	35,555.4
$R_1(7)$	35,554.0
$R_{21}(7)$	35,552.2
$R_1(3)$	35,549.4
$R_{21}(3)$	35,548.5
$R_1(8)$	35,544.0
$R_{21}(8)$	35,541.9
$R_1(2)$	35,539.0
$R_{21}(2)$	35,538.3

Peak 11	35,530
$R_1(9)$	35,529.0
$R_{21}(9)$	35,526.7
$R_1(1)$	35,526.1
$R_{21}(1)$	35,525.5

Peak 12	35,497
$R_1(10)$	35,508.9
$R_{21}(10)$	35,506.5
$R_2(7)$	35,501.0
$R_2(6)$	35,500.6
$R_2(8)$	35,495.6
$R_2(5)$	35,494.0

Peak 13	35,479
$R_2(9)$	35,484.3
$R_1(11)$	35,483.6
$R_2(4)$	35,481.1
$R_{21}(11)$	35,480.9

Peak 14	35,455
$R_2(10)$	35,467.1
$Q_1(1)$	35,461.5
$R_2(3)$	35,461.3
$Q_{21}(1)$	35,461.1

Peak 15	35,433
$R_1(12)$	35,452.8
$R_{21}(12)$	35,449.9
$R_2(11)$	35,444.2
$Q_1(2)$	35,442.1
$Q_{21}(2)$	35,441.6
$R_2(2)$	35,434.2

Peak 16	35,413
$P_1(1)$	35,429.2
$Q_1(3)$	35,420.4
$Q_{21}(3)$	35,419.6
$R_1(13)$	35,416.6
$R_2(12)$	35,415.5

Peak 17	35,391
$R_2(1)$	35,399.1
$Q_1(4)$	35,395.4
$Q_{21}(4)$	35,394.5

Peak 18	35,372
$R_2(13)$	35,380.9
$P_1(2)$	35,377.8
$R_1(14)$	35,374.6

Peak 19	35,363
$Q_1(5)$	35,366.9
$Q_{21}(5)$	35,365.7

Peak 20	35,333
$R_2(14)$	35,340.3
$Q_{12}(2)$	35,338.6
$Q_2(2)$	35,338.0
$Q_{12}(1)$	35,335.2
$Q_2(1)$	35,334.9
$Q_1(6)$	35,334.4
$Q_{12}(3)$	35,334.0
$Q_2(3)$	35,333.2
$Q_{21}(6)$	35,333.0

Peak 21	35,323
$R_1(15)$	35,326.9
$P_1(3)$	35,324.1
$Q_{12}(4)$	35,322.1
$Q_2(4)$	35,321.1

Peak 22	35,303
$Q_{12}(5)$	35,303.5
$P_{12}(1)$	35,302.7
$Q_2(5)$	35,302.3
$Q_1(7)$	35,297.6
$Q_{21}(7)$	35,296.0
$R_2(15)$	35,293.7

Peak 23	35,281
$Q_{12}(6)$	35,278.8
$Q_2(6)$	35,277.4
$P_{12}(2)$	35,273.8
$P_2(2)$	35,273.4
$P_1(4)$	35,267.6

Peak 24	35,251
$Q_1(8)$	35,256.4
$Q_{21}(8)$	35,254.6
$Q_{12}(7)$	35,248.2
$Q_2(7)$	35,246.6
$O_{12}(2)$	35,241.7
$R_2(16)$	35,241.1
$P_{12}(3)$	35,237.0
$P_2(3)$	35,236.5

Peak 25	35,208
$Q_{12}(8)$	35,212.0
$Q_1(9)$	35,210.6
$Q_2(8)$	35,210.2
$Q_{21}(9)$	35,208.6
$P_1(5)$	35,207.8

Peak 26	35,188
$P_{12}(4)$	35,193.3
$P_2(4)$	35,192.5

Peak 27	35,158
$O_{12}(3)$	35,172.7
$Q_{12}(9)$	35,170.4
$Q_2(9)$	35,168.3
$Q_1(10)$	35,160.2
$Q_{21}(10)$	35,157.9

Peak 28	35,135
$P_1(6)$	35,144.3
$P_{12}(5)$	35,143.2
$P_2(5)$	35,142.2

Peak 29	35,114
$Q_{12}(10)$	35,123.3
$Q_2(10)$	35,121.0

Peak 30	35,100
$Q_1(11)$	35,104.9
$Q_{21}(11)$	35,102.4
$O_{12}(4)$	35,096.8

Peak 31	35,083
$P_{12}(6)$	35,087.2
$P_2(6)$	35,086.0

Peak 32	35,072
$P_1(7)$	35,076.9
$Q_{12}(11)$	35,070.9
$Q_2(11)$	35,068.4

Peak 33	35,043
$Q_1(12)$	35,044.7
$Q_{21}(12)$	35,042.0

Peak 34	35,026
$P_{12}(7)$	35,025.8
$P_2(7)$	35,024.4

Peak 35	35,009
$O_{12}(5)$	35,014.5
$Q_{12}(12)$	35,013.2
$Q_2(12)$	35,010.5
$P_1(8)$	35,005.5

Peak 36	34,986
$Q_1(13)$	34,979.5
$Q_{21}(13)$	34,976.6

Peak 37	34,964
$P_{12}(8)$	34,959.1
$P_2(8)$	34,957.5
$Q_2(13)$	34,947.2

Peak 38	34,932
$P_1(9)$	34,929.9
$O_{12}(6)$	34,926.5

Peak 39	34,906
$Q_1(14)$	34,909.3
$Q_{21}(14)$	34,906.2

Peak 40	34,877
$P_{12}(9)$	34,887.5
$P_2(9)$	34,885.6
$Q_2(14)$	34,878.6

Peak 41	34,842
$P_1(10)$	34,850.2

Peak 42	34,825
$Q_1(15)$	34,834.0
$O_{12}(7)$	34,833.2
$Q_{21}(15)$	34,830.7

Peak 43	34,804
$P_{12}(10)$	34,810.9
$P_2(10)$	34,808.8
$Q_2(15)$	34,804.7

Peak 44	34,763
$R_1(5)$*	34,769.2
$R_1(4)$*	34,768.9
$P_1(11)$	34,766.2
$R_1(6)$*	34,765.1
$R_1(3)$*	34,764.5
$R_{21}(3)$*	34,763.5
$R_1(2)$*	34,756.5
$R_1(7)$*	34,756.2
$R_{21}(2)$*	34,755.8
$Q_1(16)$	34,753.5
$R_{21}(1)$*	34,745.1

Peak 45	34,729
$O_{12}(8)$	34,734.9
$P_{12}(11)$	34,729.5
$P_2(11)$	34,727.3
$Q_2(16)$	34,725.4

Peak 46	34,708
$R_2(6)$*	34,705.3
$R_2(7)$*	34,702.2
$R_2(5)$*	34,702.0
$R_1(10)$*	34,698.4
$R_{21}(10)$*	34,696.0
$R_2(8)$*	34,692.9
$R_2(4)$*	34,692.1

Peak 47	34,685
$Q_1(1)$*	34,684.4
$Q_{21}(1)$*	34,684.1
$P_1(12)$	34,677.9
$R_2(3)$*	34,675.2
$Q_1(17)$	34,667.6
$Q_1(2)$*	34,664.7
$Q_{21}(2)$*	34,664.2

Peak 48	34,644
$P_1(1)$*	34,653.8
$R_2(2)$*	34,650.7
$P_{12}(12)$	34,643.5
$Q_1(3)$*	34,642.2
$Q_{21}(3)$*	34,641.5
$P_2(12)$	34,641.0
$Q_2(17)$	34,640.6
$O_{12}(9)$	34,631.9

Peak 49	34,614
$R_2(1)$*	34,618.1
$Q_1(4)$*	34,616.2
$Q_{21}(4)$*	34,615.3

Peak 50	34,597
$P_1(2)$*	34,603.7

Peak 51	34,576
$Q_1(5)$*	34,586.3
$P_1(13)$	34,585.3
$Q_{21}(5)$*	34,585.2
$Q_1(18)$	34,576.4

Peak 52	34,542
$Q_{12}(2)$*	34,560.1
$Q_2(2)$*	34,559.5
$Q_{12}(1)$*	34,557.6
$Q_2(1)$*	34,557.3
$Q_{12}(3)$*	34,554.5
$Q_2(3)$*	34,553.8
$P_{12}(13)$	34,552.7
$Q_1(6)$*	34,552.1
$P_1(3)$*	34,551.0
$Q_2(18)$	34,550.3
$P_2(13)$	34,550.0
$Q_{12}(4)$*	34,541.5
$Q_2(4)$*	34,540.6

Peak 53	34,517
$P_{12}(1)$*	34,526.7
$O_{12}(10)$	34,524.2
$Q_{12}(5)$*	34,521.6
$Q_2(5)$*	34,520.5
$Q_1(7)$*	34,513.4
$Q_{21}(7)$*	34,511.9

Peak 54	34,486
$P_{12}(2)$*	34,498.6
$P_2(2)$*	34,498.3
$P_1(4)$*	34,495.1
$Q_2(6)$*	34,494.0
$P_1(14)$	34,488.2

Peak 55	34,456
$Q_1(8)$*	34,470.0
$O_{12}(2)$*	34,468.2
$P_{12}(3)$*	34,462.6
$P_2(3)$*	34,462.1
$Q_2(7)$*	34,461.3
$P_{12}(14)$	34,457.3
$P_2(14)$	34,454.3

Peak 56	34,439
$P_1(5)$*	34,435.5

Peak 57	34,426
$Q_{12}(8)$*	34,424.5
$Q_2(8)$*	34,422.8
$Q_1(9)$*	34,421.7
$Q_{21}(9)$*	34,419.8
$P_{12}(4)$*	34,419.4
$P_2(4)$*	34,418.7
$O_{12}(11)$	34,412.2

Peak 58	34,394
$O_{12}(3)$*	34,401.7
$P_1(15)$	34,386.8

Peak 59	34,378
$Q_2(9)$*	34,378.4
$Q_1(20)$	34,377.5
$P_1(6)$*	34,372.0
$P_{12}(5)$*	34,369.7
$P_2(5)$*	34,368.7
$Q_1(10)$*	34,368.4

*) rotational lines of the OH A-X (2,1) band

Table 2: OH A-X (1,0) and (2,1) transitions. Identification of the rotational lines of the peaks, labeled in Fig. 6. The excitation frequencies are in [cm^{-1}]. In the upper right corner: measured excitation frequency of the peak. The rotational lines are shown with the calculated excitation frequencies.

3.3 OH excitation within the A-X (2,0) and (3,1) bands

Furthermore in the excitation wavelength range of 271.0 nm to 259.0 nm (36,900 cm^{-1} to 38,610 cm^{-1}) the methane/air flame of a Bunsen burner is investigated. The gain of the image intensifier is increased because of the lower intensity of the fluorescence signal. With a symmetric-convex lens (focal length of 150 mm) the laser beam is focused about two centimetres outside the flame front / reaction zone of the Bunsen burner.
An excitation-emission spectrum of a methane/air flame displays Fig. 7. The excitation wavelength of the laser is tuned form 271.0 nm to 259.0 nm. For each line we summed up 60 laser pulses and averaged the signal intensities of the reaction zone. The laser wavelength is tuned in 0.01 nm steps. In the experiment a 1200 grooves/mm grating is used. The emission wavelength is displayed from 258 nm to 330 nm. At wavelengths higher then 330 nm no further emissions were detected.

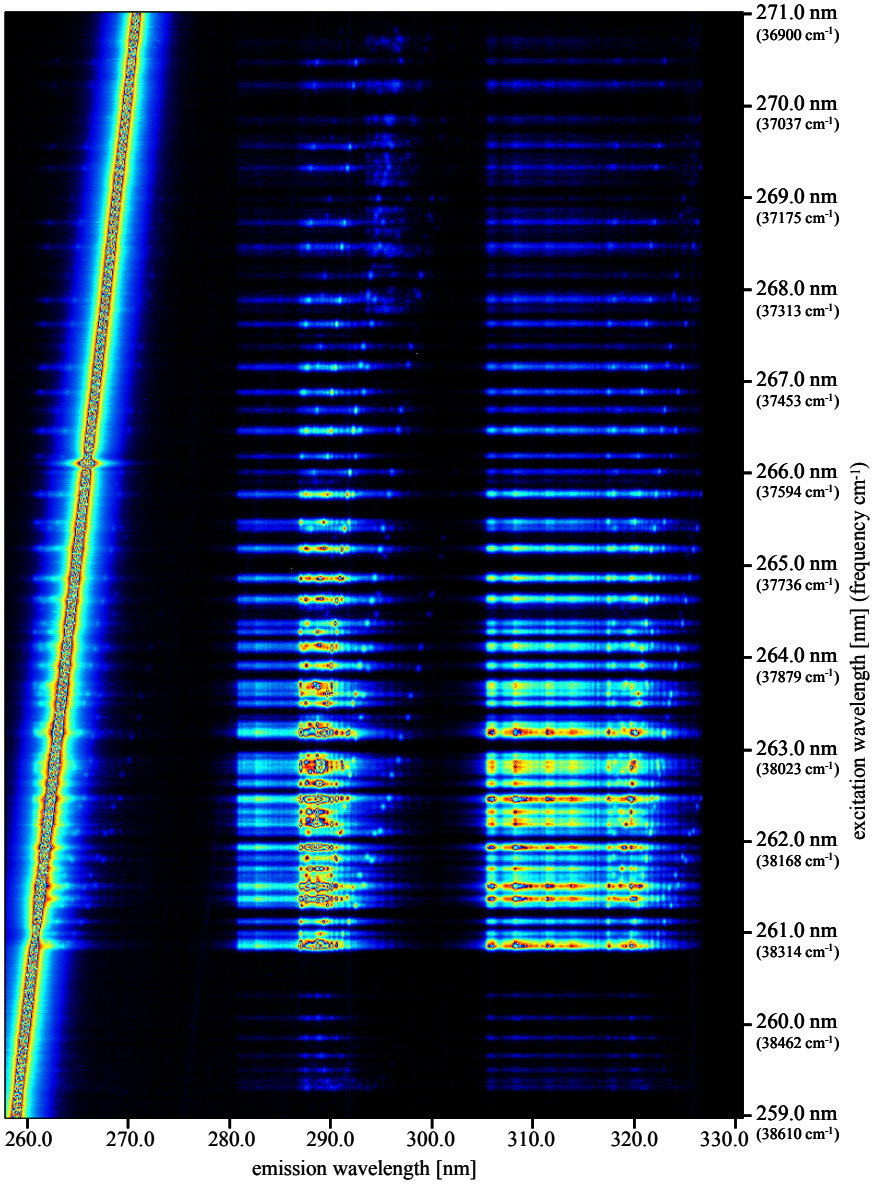

Fig. 7: Excitation-emission spectrum of a methane/air flame. The excitation wavelength is tuned from 271.0 nm to 259.0 nm. The emission wavelength is detected from 258 nm to 330 nm.

Two transition bands of OH are located within the tuned range of the laser wavelength. First there is the OH $A^2\Sigma^+$ (v' = 2) ← $X^2\Pi$ (v'' = 0) transition (laser-induced fluorescence, LIF) (Herzberg, 1971). Rotational lines start at a calculated excitation frequency of 38,553.6 cm^{-1}, transitions of the (2,0) band are found in the whole tuning range of Fig. 7 (Luque and Crosley, 1999). Second hydroxyl radicals of the flame can be excited in the $A^2\Sigma^+$ (v' = 3) ← $X^2\Pi$ (v'' = 1) transition (laser-induced predissociative fluorescence, LIPF). The excitation in the (3,1) band is predissociative and in comparison to the (2,0) band the signals are of low intensity (Luque and Crosley, 1999).
In the left part of Fig. 7 Rayleigh scattering (slope) and superposition of Rayleigh scattering and OH fluorescence in the $(2 \rightarrow 0)$ and $(3 \rightarrow 1)$ bands occur. The line of the elastic Rayleigh scattering signal starts at an emission wavelength of 271.0 nm at the upper side of the figure and ends at an emission wavelength of 259.0 nm at the bottom, respectively to the excitation wavelength of the laser. The middle section shows LIF of the $(1 \rightarrow 0)$, $(2 \rightarrow 1)$ and $(3 \rightarrow 2)$ bands. Detected emissions between 305 nm and 330 nm are from $(0 \rightarrow 0)$, $(1 \rightarrow 1)$, $(2 \rightarrow 2)$ and $(3 \rightarrow 3)$ transitions.
Fig. 8 shows an excitation spectrum of OH in a methane/air flame within the excitation wavelength range of 271.0 nm to 259.0 nm. LIF and LIPF signals are averaged in the emission wavelength interval from 286.5 nm to 290.7 nm. The figure shows the range of the $A^2\Sigma^+ \leftarrow X^2\Pi$ (2,0) transitions, starting at an excitation frequency of

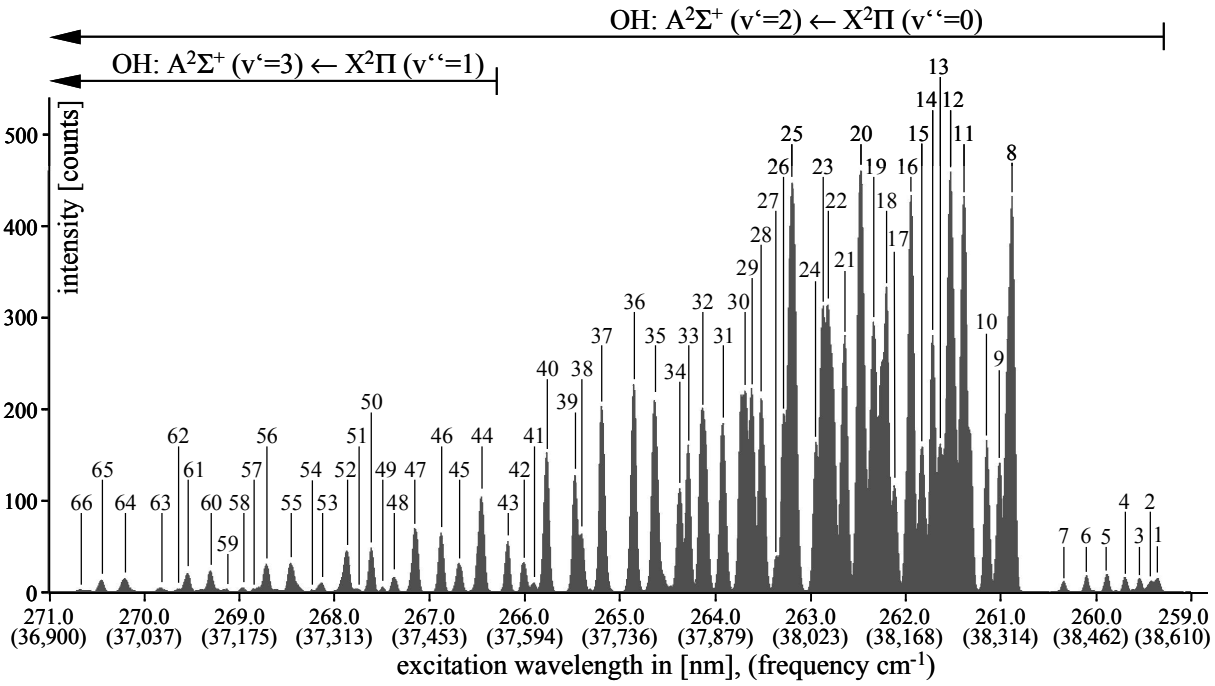

Fig. 8: Excitation spectrum of hydroxyl in a methane/air flame. The excitation wavelength ranges from 271.0 nm to 259.0 nm. The fluorescence signals are averaged in the emission wavelength interval from 286.5 nm to 290.7 nm. The rotational lines of labeled peaks are shown in Table 3.

38,533.6 nm and the range of the $A^2\Sigma^+ \leftarrow X^2\Pi$ (3,1) transitions, starting at an excitation frequency of 37,536.9 nm. The most important peaks are labeled in Fig. 8.

Table 3 shows the identification of the rotational lines of the peaks, labeled in Fig. 8 (Luque and Crosley, 1999). Also in the excitation range of the OH A-X (2,0) or (3,1) transitions, in most cases it is not possible to excite single rotational lines, the reason is the bandwidth of the laser of about 8 cm^{-1}. Thus most peaks in Fig. 8 display simultaneous excitation of several rotational lines of the hydroxyl radical.

For all peaks in Table 3 applies: The upper right corner shows the measured maximum intensity of the peak in [cm^{-1}]. All calculated rotational lines are given in [cm^{-1}]. Rotational lines with high intensity, e.g. at least 50 percent of the most intense line of this peak, are printed in bold face and with a grey background. The lines with an intensity between 50 and 10 percent of the most intense line of this peak, are printed in bold face. Rotational lines with an intensity between 10 and 2 percent of the most intense line of this peak, are printed italic. Finally, rotational lines with an intensity of less than 2 percent are not shown. For the calculation the rotational temperature T_{rot} is 2800 K and the vibrational temperature T_{vib} amounts to 2800 K.

Transitions with the highest measured intensity are the peaks labeled 8, 11, 12, 16, 20 and 25. Within the $A^2\Sigma^+$ (v' = 2) $\leftarrow X^2\Pi$ (v'' = 0) excitation, this peaks are particularly suited to excite OH radicals by an OPO (Type II) laser and to display an image of a qualitative OH distribution.

For 2-dimensional spatial-resolved OH distribution measurements it is necessary to separate the OH LIF signals from Rayleigh scattering signals with adequate filters. In the emission wavelength range from 255 nm to 275 nm superposition of Rayleigh scattering and OH fluorescence in the ($2 \rightarrow 0$) and ($3 \rightarrow 1$) bands is detected. The signals of this bands can not be used for spatial OH detection. The high intensity of the emissions in the ($3 \rightarrow 2$), ($2 \rightarrow 1$) and ($1 \rightarrow 0$) bands (emission wavelength from about 280 nm to 300 nm), as well as the emissions in the ($3 \rightarrow 3$), ($2 \rightarrow 2$), ($1 \rightarrow 1$) and ($0 \rightarrow 0$) bands (emission wavelength from about 305 nm to 325 nm) allow measurements of the quantitative distribution of hydroxyl radicals in flames.

Peak 1	38,559
$S_{21}(8)$	38,553.6
$S_{21}(7)$	38,551.3
$S_{21}(9)$	38,548.7

Peak 2	38,549
$S_{21}(6)$	38,542.1
$S_{21}(10)$	38,536.4

Peak 3	38,531
$S_{21}(5)$	38,526.2
$S_{21}(11)$	38,516.5

Peak 4	38,507
$S_{21}(4)$	38,504.0

Peak 5	38,481
$S_{21}(12)$	38,488.8
$S_{21}(3)$	38,476.0

Peak 6	38,448
$S_{21}(2)$	38,442.7

Peak 7	38,413
$S_{21}(1)$	38,404.9

Peak 8	38,333
$R_1(3)$	38,325.6
$R_{21}(3)$	38,324.7
$R_1(4)$	38,324.4
$R_{21}(4)$	38,323.3
$R_1(2)$	38,322.0
$R_{21}(2)$	38,321.3
$R_1(5)$	38,317.7
$R_{21}(5)$	38,316.4
$R_1(1)$	38,314.1
$R_{21}(1)$	38,313.6

Peak 9	38,314
$R_1(6)$	38,305.1
$R_{21}(6)$	38,303.6

Peak 10	38,294
$R_1(7)$	38,286.4
$R_{21}(7)$	38,284.6

Peak 11	38,258
$R_1(8)$	38,261.2
$R_{21}(8)$	38,259.2
$Q_1(1)$	38,252.9
$Q_{21}(1)$	38,252.6
$R_2(5)$	38,251.8
R2(4)	38,248.9
$R_2(6)$	38,246.5

Peak 12	38,238
$R_2(3)$	38,237.6
$R_2(7)$	38,233.5
$Q_1(2)$	38,230.2
$Q_{21}(2)$	38,229.7
$R_1(9)$	38,229.3
$R_{21}(9)$	38,227.1

Peak 13	38,222
$P_1(1)$	38,222.3
$R_2(2)$	38,217.2
$R_2(8)$	38,212.8

Peak 14	38,210
$Q_1(3)$	38,203.3
$Q_{21}(3)$	38,202.6

Peak 15	38,194
$R_1(10)$	38,190.6
$R_{21}(10)$	38,188.3
$R_2(1)$	38,187.1
$R_2(9)$	38,184.6

Peak 16	38,177
$Q_1(4)$	38,171.7
$Q_{21}(4)$	38,170.7
$P_1(2)$	38,169.2

Peak 17	38,152
$R_2(10)$	38,149.0
$R_1(11)$	38,145.0
$R_{21}(11)$	38,142.4

Peak 18	38,140
$Q_1(5)$	38,134.7
$Q_{21}(5)$	38,133.6
$Q_{12}(1)$	38,126.6
$Q_{12}(2)$	38,126.6
$Q_2(1)$	38,126.3
$Q_2(2)$	38,126.1

Peak 19	38,120
$Q_{12}(3)$	38,116.9
$Q_2(3)$	38,116.2
$P_1(3)$	38,112.2
$R_2(11)$	38,105.8

Peak 20	38,101
$Q_{12}(4)$	38,098.3
$Q_2(4)$	38,097.4
$P_{12}(1)$	38,095.8
$R_1(12)$	38,092.3
$Q_1(6)$	38,092.1
$Q_{21}(6)$	38,090.7

Peak 21	38,076
$Q_{12}(5)$	38,071.3
$Q_2(5)$	38,070.2
$P_{12}(2)$	38,065.2
$P_2(2)$	38,064.9

Peak 22	38,050
$R_2(12)$	38,055.0
$P_1(4)$	38,050.6

Peak 23	38,043
$Q_1(7)$	38,043.5
$Q_{21}(7)$	38,041.9
$Q_{12}(6)$	38,036.5
$Q_2(6)$	38,035.1
$O_{12}(2)$	38,034.8
$R_1(13)$	38,032.3

Peak 24	38,031
$P_{12}(3)$	38,025.1
$P_2(3)$	38,024.5

Peak 25	37,995
$R_2(13)$	37,996.7
$Q_{12}(7)$	37,994.1
$Q_2(7)$	37,992.5
$Q_1(8)$	37,988.8
$Q_{21}(8)$	37,987.0
$P_1(5)$	37,984.0

Peak 26	37,982
$P_{12}(4)$	37,976.2
$P_2(4)$	37,975.5

Peak 27	37,972
$R_1(14)$	37,965.0
$O_{12}(3)$	37,964.2

Peak 28	37,949
$Q_{12}(8)$	37,944.4
$Q_2(8)$	37,942.6

Peak 29	37,935
$R_2(14)$	37,930.8
$Q_1(9)$	37,927.8
$Q_{21}(9)$	37,925.9

Peak 30	37,922
$P_{12}(5)$	37,919.4
$P_2(5)$	37,918.5
$P_1(6)$	37,912.0

Peak 31	37,892
$Q_{12}(9)$	37,887.5
$Q_2(9)$	37,885.6
$O_{12}(4)$	37,884.8

Peak 32	37,862
$Q_1(10)$	37,860.5
$Q_{21}(10)$	37,858.3
$P_{12}(6)$	37,855.0
$P_2(6)$	37,853.8

Peak 33	37,839
$P_1(7)$	37,834.5

Peak 34	37,826
$Q_{12}(10)$	37,823.6
$Q_2(10)$	37,821.4

Peak 35	37,789
$O_12(5)$	37,797.5
$Q_1(11)$	37,786.6
$Q_{21}(11)$	37,784.2
$P_{12}(7)$	37,783.4
$P_2(7)$	37,782.1

Peak 36	37,756
$Q_{12}(11)$	37,752.6
$P_1(8)$	37,751.3
$Q_2(11)$	37,750.2

Peak 37	37,709
$Q_1(12)$	37,706.1
$P_{12}(8)$	37,705.0
$P_2(8)$	37,703.4
$O_{12}(6)$	37,702.8

Peak 38	37,679
$Q_{12}(12)$	37,674.6
$Q_2(12)$	37,672.0

Peak 39	37,669
$P_1(9)$	37,662.3

Peak 40	37,627
$P_12(9)$	37,619.8
$Q_1(13)$	37,619.0
$P_2(9)$	37,618.1

Peak 41	37,607
$O_{12}(7)$	37,601.0

Peak 42	37,593
$Q_{12}(13)$	37,589.6
$Q_2(13)$	37,586.8

Peak 43	37,569
$P_1(10)$	37,567.4

Peak 44	37,529
$P_{12}(10)$	37,528.1
$P_2(10)$	37,526.1
$Q_1(14)$	37,525.1

Peak 45	37,497
$Q_{12}(14)$	37,497.5
$Q_2(14)$	37,494.5
$O_{12}(8)$	37,492.6

Peak 46	37,470
$P_1(11)$	37,466.5

Peak 47	37,432
$P_{12}(11)$	37,429.8
$P_2(11)$	37,427.7
$Q_1(15)$	37,424.4

Peak 48	37,400
$Q_{12}(15)$	37,398.4
$Q_2(15)$	37,395.2

Peak 49	37,383
$O_{12}(9)$	37,377.7

Peak 50	37,366
$P_1(12)$	37,359.6

Peak 51	37,347
$R_1(3)$*	37,340.7
$R_{21}(3)$*	37,339.8
$R_1(2)$*	37,339.7
$R_{21}(2)$*	37,339.0
$R_1(4)$*	37,336.5
$R_{21}(4)$*	37,335.4
$R_1(1)$*	37,334.0
$R_{21}(1)$*	37,333.5

Peak 52	37,330
$P_{12}(12)$	37,325.2
$P_2(12)$	37,322.8
$Q_1(16)$	37,316.7

Peak 53	37,295
$Q_{12}(16)$	37,292.1
$Q_2(16)$	37,288.7
$R_1(7)$*	37,287.4

Peak 54	37,280
$Q_1(1)$*	37,276.2
$Q_{21}(1)$*	37,275.9
$R_1(21)$	37,274.3

Peak 55	37,249
$O_{12}(10)$	37,256.6
$P_1(13)$	37,246.7

Peak 56	37,213
$Q_1(3)$*	37,225.3
$P_{12}(13)$	37,214.1
$P_2(13)$	37,211.5
$Q_1(17)$	37,201.9

Peak 57	37,195
$Q_{21}(17)$	37,198.3
$P_1(2)$*	37,195.5
$Q_1(4)$*	37,192.4
$Q_{21}(4)$*	37,191.5

Peak 58	37,179
$Q_{12}(17)$	37,178.7
$R_1(10)$*	37,177.3
$R_2(9)$*	37,175.6
$Q_2(17)$	37,175.0

Peak 59	37,155
$Q_1(5)$*	37,153.9
$Q_{21}(5)$*	37,152.8
$Q_{12}(1)$*	37,149.4
$Q_2(1)$*	37,149.1
$Q_{12}(2)$*	37,148.4
$Q_2(2)$*	37,147.9

Peak 60	37,132
$P_1(3)$*	37,139.4
$Q_2(3)$*	37,137.0
$O_{12}(11)$	37,129.3
$P_1(14)$	37,127.7
$Q_2(4)$*	37,116.8

Peak 61	37,100
$Q_1(6)$*	37,109.3
$P_{12}(14)$	37,096.7
$P_2(14)$	37,093.9
$Q_2(5)$*	37,088.1

Peak 62	37,088
$Q_1(18)$	37,080.0
$P_1(4)$*	37,078.2

Peak 63	37,059
$R_1(12)$*	37,067.3
$O_{12}(2)$*	37,061.8
$Q_1(7)$*	37,058.5
$Q_{21}(7)$*	37,057.0
$Q_2(18)$	37,054.1
$Q_{12}(6)$*	37,052.5
$Q_2(6)$*	37,051.2
$P_{12}(3)$*	37,051.0
$P_2(3)$*	37,050.5

Peak 64	37,008
$P_1(5)$*	37,011.8
$Q_2(7)$*	37,006.5
$P_1(15)$	37,002.5
$P_2(4)$*	37,001.9
$Q_1(8)$*	37,001.2
$O_{12}(12)$	36,996.1

Peak 65	36,974
$P_{12}(15)$	36,972.9
$P_2(15)$	36,969.9

Peak 66	36,942
$Q_{12}(8)$*	36,955.7
$Q_2(8)$*	36,954.0
$Q_1(19)$	36,950.9
$P_{12}(5)$*	36,945.9
$P_2(5)$*	36,945.0
$P_1(6)$*	36,939.6
$Q_1(9)$*	36,937.3
$Q_{21}(9)$*	36,935.4
$R_1(14)$*	36,926.4
$Q_2(19)$	36,925.7

*) rotational lines of the OH A-X (3,1) band

Table 3: OH A-X (2,0) and (3,1) transitions. Identification of the rotational lines of the peaks, labeled in Fig. 8. The excitation frequencies are in [cm^{-1}]. In the upper right corner: measured excitation frequency of the peak. The rotational lines are shown with the calculated excitation frequencies.

3.4 OH excitation within the A-X (3,0) band

In the range of 251.1 nm down to 242.1 nm preliminary investigations with methane/air flames showed that the fluorescence signals of diverse molecules and radicals are weak because of the low pulse energy of about 5 mJ of the laser. In order to get higher temperatures and correspondingly a higher OH number density, further experiments are done with a hydrogen/oxygen flame of a welding torch. With a symmetric-convex lens, focal length of 150 mm, the laser beam is focused about two centimetres outside the flame front / reaction zone of the flame of the welding torch.

Fig. 9 displays the excitation-emission spectrum (EES) of the hydrogen/oxygen flame. The excitation wavelength of the laser is tuned from 251.1 nm to 242.1 nm (39,825 cm^{-1} to 41,305 cm^{-1}) and the detected emission wavelength in the EES reaches form 224 nm to 298 nm. In the experiment we summed up 60 laser pulses for each line of the figure and averaged the signal intensities of the reaction zone. The laser wavelength is tuned in 0.01 nm steps. The tuning range of the KrF excimer laser, 248.9 nm to 247.7 nm (40,176.8 cm^{-1} to 40,375 cm^{-1}), is situated within the scanned area.

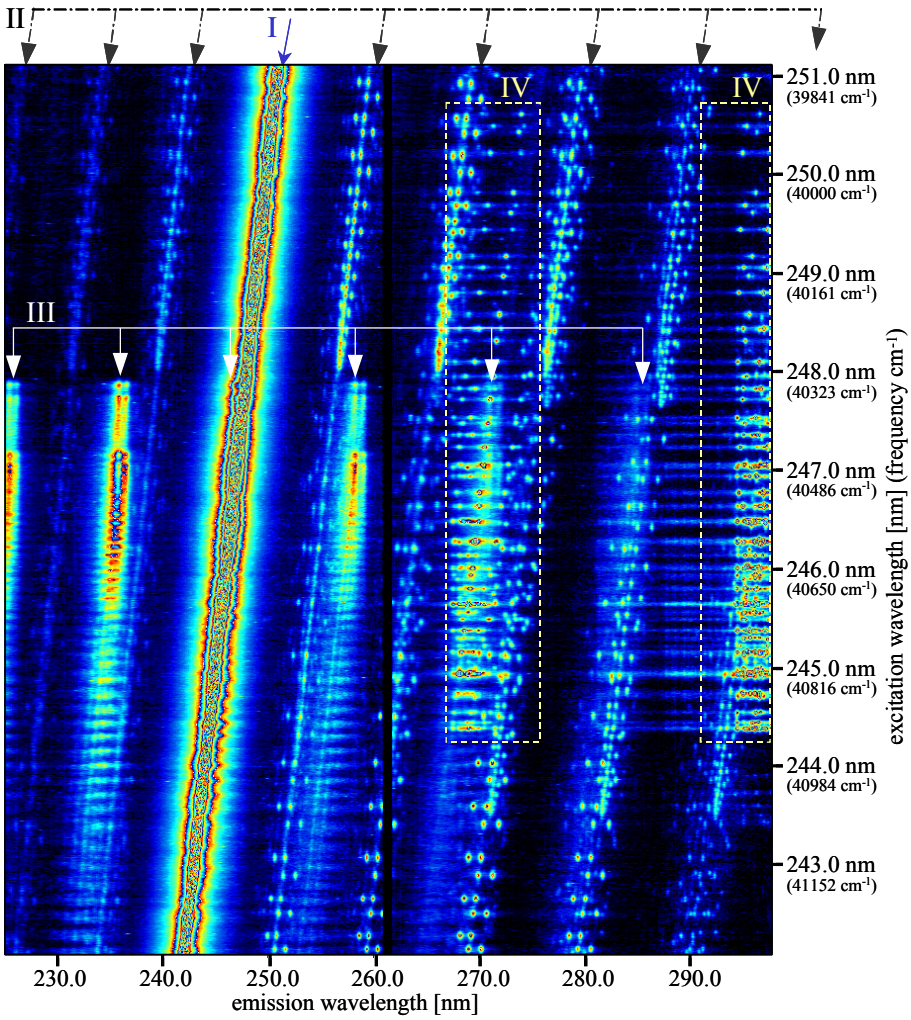

Fig. 9: Excitation-emission spectrum of a hydrogen/oxygen flame. The excitation wavelength is tuned from 251.1 nm until 242.1 nm. The emission wavelength is detected from 224 nm to 300 nm

In the excitation-emission spectrum of Fig. 9 different signals are detected: Rayleigh scattering, LIF and LIPF. The line of the elastic Rayleigh scattering (labeled I) starts at an emission wavelength of 251.1 nm at the upper side of the figure and ends at an emission wavelength of 242.1 nm at the bottom respectively to the excitation wavelength of the laser. Rayleigh scattering interferes with fluorescence signals of diverse molecules and radicals.

At the upper edge of Fig. 9 (excitation frequency of about 39.850 cm^{-1}) vibrational bands at ≈226 nm, ≈233 nm, ≈241 nm, ≈259 nm, ≈268 nm, ≈279 nm and ≈289 nm are detected. These emissions, labeled II, parallel to the Rayleigh line are transitions from Schumann-Runge bands of molecular oxygen O_2. They correspond to the transitions from the ground state $^3\Sigma_g^-$ to the higher electronic state $^3\Sigma_u^-$ ($B^3\Sigma_u^- \leftarrow X^3\Sigma_g^-$). The electronic B state $^3\Sigma_u^-$ is predissociative (Herzberg,1967).

In the experiment ambient air mixes into the hydrogen/oxygen flame and thus nitrogen oxide is formed. In the range investigated, there are several rotational lines of the $A^2\Sigma^+ \leftarrow X^2\Pi$ (0,2) and (1,3) transitions of nitrogen monoxide (Frodermann, 1996). Fig. 9 shows NO $A^2\Sigma^+ \leftarrow X^2\Pi$ (0,2) and (1,3) laser-induced fluorescence, labeled III, starting at a laser excitation frequency of about 40,330 cm^{-1}. In (Stocker et al., 2000) it is shown, that with an OPO (Type II) laser system, it is possible to excite NO at specified wavelength selectively.

In area labeled IV of Fig. 9 (rectangular broken lines) laser-induced predissociative fluorescence LIPF of hydroxyl $A^2\Sigma^+$ (v' = 3) ← X $^2\Pi$ (v'' = 0) transitions are detected (Frodermann, 1996) (Herzberg, 1971). In the left

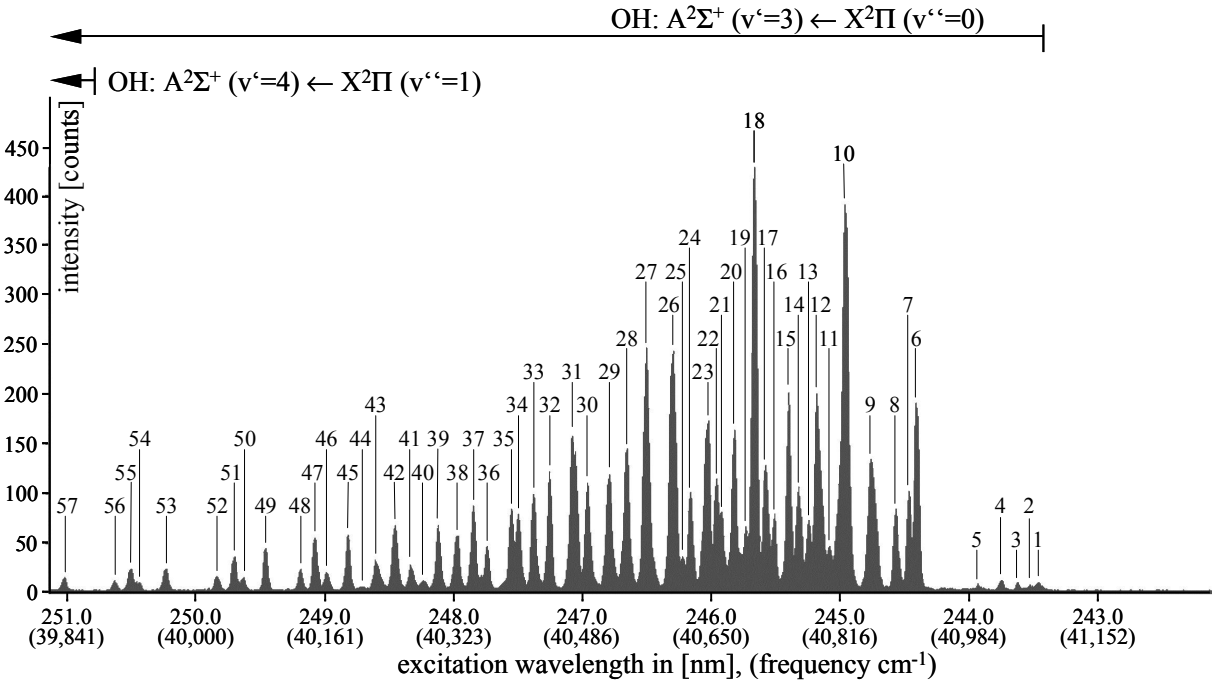

Fig. 10: Excitation spectrum of hydroxyl in a hydrogen/oxygen flame. The excitation wavelength ranges from 251.1 nm to 242.1 nm. The fluorescence signals are averaged in the emission wavelength interval from 294.0 nm to 297.5 nm. The rotational lines of labeled peaks are shown in Table 4.

rectangle OH LIPF $A^2\Sigma^+ \rightarrow X^2\Pi$ of (3,1) and (2,0) band transitions are shown. The lower vibrational levels are populated by vibrational energy transfer (VET) after excitation. In the upper left corner and lower right corner, LIPF of hot oxygen (Schumann-Runge bands) superposes OH fluorescence. Starting at a laser excitation frequency of about 40,330 cm^{-1}, NO LIF superposes OH LIPF. The right rectangle of area III shows hydroxyl laser-induced predissociative fluorescence $A^2\Sigma^+ \rightarrow X^2\Pi$ of (3,2), (2,1) and (1,0) bands. In addition, this OH fluorescence signals interfere with hot oxygen LIPF and NO LIF.

Fig. 10 displays an excitation spectrum of OH $A^2\Sigma^+ \leftarrow X\ ^2\Pi$ (3,0) and (4,1) transitions in a hydrogen/oxygen flame within the excitation wavelength range from 251.1 nm to 242.1 nm. The fluorescence signals are averaged in the emission wavelength interval from 294.0 nm to 297.5 nm. Because of the laser bandwidth of about 8 cm^{-1} it is in most cases not possible to excite single rotational lines of the OH $A^2\Sigma^+ \leftarrow X^2\Pi$ (3,0) and (4,1) transitions. Thus the peaks in Fig. 10 display simultaneous excitation of several rotational lines of OH. The most important peaks are labeled in the figure.

The transitions within the tuning range of the EES are identified with the program LIFBASE (SRI International) (Luque and Crosley, 1999). Table 4 shows the identification of the rotational lines of the peaks, labeled in Fig. 10. For all peaks in Table 4 applies: The upper right corner shows the measured maximum intensity of the peak in [cm^{-1}]. All calculated rotational lines are given in [cm^{-1}]. Rotational lines with high intensity, e.g. at least 50 percent of the most intense line of this peak, are printed in bold face and with a grey background. The lines with an intensity between 50 and 10 percent of the most intense line of this peak, are printed in bold face. Rotational lines with an intensity between 10 and 2 percent of the most intense line of this peak, are printed italic. Finally, rotational lines with an intensity of less than 2 percent are not shown. For the calculation the rotational temperature T_{rot} and the vibrational temperature T_{vib} amount to 2200 K.

Due to the interference of OH $A^2\Sigma^+$ (v' = 3) $\leftarrow X^2\Pi$ (v'' = 0) transitions with O_2 LIPF or NO LIF within the excitation range, it is not possible to excite OH radicals selectively with the OPO (Type II) laser system. Only in cases with no NO formation or in absence of hot oxygen it is possible to detect OH selectively. Nevertheless the OH fluorescence signals of the A-X (3,0) transitions, excited by an OPO (Type II) laser, are weak.

Peak 1	41,073
$S_{21}(6)$	41,073.4
$S_{21}(5)$	41,071.3
$S_{21}(7)$	41,067.0

Peak 2	41,061
$S_{21}(4)$	41,061.3

Peak 3	41,068
$S_{21}(8)$	41,051.8
$S_{21}(3)$	41,043.6

Peak 4	41,024
$S_{21}(9)$	41,027.7
$S_{21}(2)$	41,019.0

Peak 5	40,994
$S_{21}(10)$	*40,994.4*
$S_{21}(1)$	40,988.1

Peak 6	40,913
$R_1(2)$	40,905.1
$R_{21}(2)$	40,904.5
$R_1(1)$	40,902.5
$R_{21}(1)$	40,902.0
$R_1(3)$	40,901.9
$R_{21}(3)$	40,901.0

Peak 7	40,903
$R_1(4)$	40,892.0
$R_{21}(4)$	40,890.9

Peak 8	40,886
$R_1(5)$	40,874.9
$R_{21}(5)$	40,873.6

Peak 9	40,855
$R_1(6)$	40,850.2
$R_{21}(6)$	40,848.7
$Q_1(1)$	40,844.7
$Q_{21}(1)$	40,844.4

Peak 10	40,821
$Q_1(2)$	40,818.5
$Q_{21}(2)$	40,818.0
$R_1(7)$	40,817.5
$R_2(4)$	40,816.6
$R_{21}(7)$	*40,815.8*
$P_1(1)$	40,815.8
$R_2(3)$	40,813.9
$R_2(5)$	40,809.0

Peak 11	40,801
$R_2(2)$	40,800.4

Peak 12	40,785
$R_2(6)$	40,791.6
$Q_1(3)$	40,786.5
$Q_{21}(3)$	40,785.8

Peak 13	40,775
$R_1(8)$	40,776.7
$R_2(1)$	40,775.5
$R_{21}(8)$	40,774.8

Peak 14	40,761
$R_2(7)$	40,764.7
$P_1(2)$	40,761.0

Peak 15	40,748
$Q_1(4)$	40,747.9
$Q_{21}(4)$	40,747.0

Peak 16	40,730
$R_2(8)$	40,728.4
$R_1(9)$	40,727.4
$R_{21}(9)$	*40,725.4*

Peak 17	40,718
$Q_{12}(1)$	40,718.4
$Q_2(1)$	40,718.1
$Q_{12}(2)$	40,715.0
$Q_2(2)$	40,714.5

Peak 18	40,705
$Q_1(5)$	40,702.3
$Q_{21}(5)$	40,701.2
$P_1(3)$	40,700.5
$Q_{12}(3)$	40,700.1
$Q_2(3)$	40,699.4

Peak 19	40,693
$P_{12}(1)$	40,689.4
$R_2(9)$	40,682.9

Peak 20	40,679
$Q_{12}(4)$	40,674.5
$Q_2(4)$	40,673.6
$R_1(10)$	40,669.6

Peak 21	40,662
$P_{12}(2)$	40,657.0
$P_2(2)$	40,656.7

Peak 22	40,655
$Q_1(6)$	40,649.2
$Q_{21}(6)$	*40,648.0*

Peak 23	40,645
$Q_{12}(5)$	40,638.9
$Q_2(5)$	40,637.8
$P_1(4)$	40,633.8
$O_{12}(2)$	*40,628.3*
$R_2(10)$	40,628.0

Peak 24	40,622
$P_{12}(3)$	40,613.4
$P_2(3)$	40,612.9

Peak 25	40,612
$R_1(11)$	40,603.0
$R_{21}(11)$	40,600.5

Peak 26	40,601
$Q_{12}(6)$	*40,593.7*
$Q_2(6)$	40,592.4
$Q_1(7)$	40,588.5
$Q_{21}(7)$	*40,587.1*

Peak 27	40,566
$R_2(11)$	40,563.8
$P_1(5)$	40,560.2
$P_{12}(4)$	40,559.4
$P_2(4)$	40,558.7
$O_{12}(3)$	40,556.0

Peak 28	40,542
$Q_{12}(7)$	*40,539.2*
$Q_2(7)$	40,537.7

Peak 29	40,519
$R_1(12)$	*40,527.4*
$Q_1(8)$	40,520.0
$Q_{21}(8)$	*40,518.3*

Peak 30	40,491
$P_{12}(5)$	40,495.6
$P_2(5)$	40,494.7
$R_2(12)$	40,490.3

Peak 31	40,473
$P_1(6)$	40,479.6
$Q_{12}(8)$	*40,475.6*
$Q_2(8)$	40,473.9
$O_{12}(4)$	40,473.2

Peak 32	40,443
$Q_1(9)$	40,443.3
$R_1(13)$	*40,442.8*
$Q_{21}(9)$	*40,441.5*

Peak 33	40,420
$P_{12}(6)$	40,422.6
$P_2(6)$	40,421.5

Peak 34	40,404
$R_2(13)$	*40,407.4*
$Q_{12}(9)$	*40,403.1*
$Q_2(9)$	40,401.2

Peak 35	40,394
$P_1(7)$	40,391.7
$O_{12}(5)$	40,380.7

Peak 36	40,365
$Q_1(10)$	40,358.6
$Q_{21}(10)$	*40,356.5*

Peak 37	40,347
$R_1(14)$	*40,349.0*
$P_{12}(7)$	40,340.6
$P_2(7)$	40,339.3

Peak 38	40,327
$Q_{12}(10)$	*40,321.7*
$Q_2(10)$	40,319.6
$R_2(14)$	*40,314.9*

Peak 39	40,303
$P_1(8)$	40,296.4

Peak 40	40,284
$O_{12}(6)$	40,279.0

Peak 41	40,267
$Q_1(11)$	40,265.5
$Q_{21}(11)$	*40,263.3*

Peak 42	40,248
$P_{12}(8)$	40,250.0
$P_2(8)$	40,248.5

Peak 43	40,224
$Q_{12}(11)$	*40,231.5*
$Q_2(11)$	40,229.3

Peak 44	40,207
$R_2(15)$	40,212.8

Peak 45	40,190
$P_1(9)$	40,193.5

Peak 46	40,162
$O_{12}(7)$	40,168.6
$Q_1(12)$	40,164.1
$Q_{21}(12)$	*40,161.6*

Peak 47	40,148
$P_{12}(9)$	40,151.0
$P_2(9)$	40,149.3

Peak 48	40,130
$R_1(16)$	*40,132.8*
$Q_{12}(12)$	*40,132.5*
$Q_2(12)$	40,130.1

Peak 49	40,087
$P_1(11)$	40,082.9

Peak 50	40,059
$Q_1(13)$	40,054.1
$Q_{21}(13)$	*40,051.5*
$O_{12}(8)$	40,049.8

Peak 51	40,048
$P_{12}(10)$	*40,043.6*
$P_2(10)$	40,041.7

Peak 52	40,026
$Q_{12}(13)$	*40,024.7*
$Q_2(13)$	40,022.1

Peak 53	39,963
$P_1(11)$	39,964.6

Peak 54	39,930
$Q_1(14)$	39,935.6
$Q_{21}(14)$	*39,932.7*

Peak 55	39,920
$P_{12}(11)$	*39,928.0*
$P_2(11)$	39,925.9
$O_{12}(9)$	*39,922.8*

Peak 56	39,899
$Q_{12}(14)$	*39,908.0*
$Q_2(14)$	39,905.2

Peak 57	39,837
$P_1(12)$	39,838.6

Table 4: OH A-X (3,0) transitions. Identification of the rotational lines of the peaks, labeled in Fig. 10. The excitation frequencies are in [cm^{-1}]. In the upper right corner: measured excitation frequency of the peak. The rotational lines are shown with the calculated excitation frequencies.

4. CONCLUSION

The presented investigations outline the possibilities of OH detection in methane/air and hydrogen/oxygen flames with a tunable OPO (Type II) laser system by means of laser-induced fluorescence (LIF) and laser-induced predissociative fluorescence (LIPF). For selective OH detection it is important to obtain high signal intensities and there should be no fluorescence signal superposition of other molecules. In order to find appropriate electronic transitions, the excitation wavelength range from 325 nm to 240 nm (excitation frequency: 30,769 cm^{-1} to 41,667 cm^{-1}) was scanned. The transitions of the hydroxyl radical $A^2\Sigma^+ \leftarrow X^2\Pi$ (0,0), (1,1), (2,2), (1,0), (2,1), (2,0), (3,1) and (3,0) bands have been excited and investigated more intensely.

The experiments show, that selective OH excitation with an OPO (Type II) laser is best suited within the OH A-X (0,0), (1,0) and (2,0) bands. Within this bands the fluorescence signal intensities of methane/air and hydrogen/oxygen flames are high enough for detection of OH. In most cases there is no superposition of various molecules. However, with an excitation within the (0,0), (1,0) and (2,0) bands only qualitative measurements of hydroxyl distribution can be obtained, because of quenching.

Within the excitation range of the OH A-X (3,0) band selective excitation of hydroxyl is only possible if there is no nitric oxide formation and if there is no hot oxygen present.
A comparison of OH fluorescence signal intensities shows that excitation within the $A^2\Sigma^+ \leftarrow X^2\Pi$ (0,0) band (LIF) yields about four hundred times stronger signal intensities than excitation within the (3,0) band (excitation range of the KrF excimer laser, OH LIPF). The excitation within the (1,0) band (LIF) yields about one hundred times stronger and excitation within the (2,0) band (LIF) yields about twenty times stronger fluorescence signal intensities compared to the (3,0) band of OH (LIPF).
Because of the high level of OH fluorescence signal intensities in the OH A-X (0,0), (1,0) and (2,0) bands it is possible to get spatial and time-resolved measurements of the OH distribution in flames. Fig. 1 shows an OH LIF single shot measurement in a methane/air flame of a Bunsen burner at a measured excitation frequency of 38,333 cm^{-1}. Further investigations will aim at spatial-resolved and time-resolved images of the OH distribution in industrial burners.

REFERENCES

Arnold A., Becker H., Hemberger R., Hentschel W., Kollner K., Meienburg W., Monkhouse P., Neckel H., Schafer M., Schindler K. P., Sick V., Suntz R., and Wolfrum J., 1990, "Laser in situ monitoring of combustion processes", Applied Optics Vol. 29, 4860-4872.

Bormann F. C., Nielsen T., Burrows M., and Andresen P., 1997, "Picosecond planar laser-induced fluorescence measurements of OH $A^2\Sigma^+$ (v' = 2) lifetime and energy transfer in atmospheric pressure flames", Applied Optics Vol. 36, 6129-6140.

Brockhinke A., Kreutner W., Rahmann U., Kohse-Höinghaus K., Settersten T. B., and Linne M. A., 1999, "Time-, wavelength-, and polarization-resolved measurements of OH ($A^2\Sigma^+$) picosecond laser-induced fluorescence in atmospheric-pressure flames", Appl. Phys. B 69,477-485.

Dreizler A., Tadday R., Monkhouse P., and Wolfrum J., 1993, "Time and spatially resolved LIF of OH $A^2\Sigma^+$ (v' = 1) in atmospheric-pressure flames using picosecond excitation", Appl. Phys. B 57,85-87.

Eckbreth A. C., 1996, "Laser Diagnostics for Combustion Temperature and Species", Gordon and Breach Science Publishers SA.

Frodermann M., 1996, "UV-laserspektroskopische Untersuchungen mit einem abstimmbaren Krypton-Fluorid Excimerlaser an laminaren, vorgemsichten Kohlenwasserstoff-Flammen", Ph.D. dissertation, Bielefeld University, Bielefeld, Germany.

Herzberg G., 1967, "Molecular Spectra and Molecular Structure: 1. Spectra of Diatomic Molecules", D. Van Nostrand Company, Inc.

Herzberg G., 1971, "The Spectra and Structures of Simple Free Radicals", Cornell University Press.

Kobayashi H., Oyachi Y., and Maruta K., 1999, "LIF measurements of turbulent premixed flames in a high pressure environment", Proceedings of the 5th ASME/JSME Joint Thermal Eng. Conf., AJTE99-6480.

Koch A., Chryssostomou A., Andresen P., and Bornscheuer W., 1993, "Multi-species detection in spray flames with tunable excimer lasers", Appl. Phys. B 56, 165-176.

Kohse-Höinghaus K., 1994, "Laser techniques for the quantitative detection of reactive intermediates in combustion systems", Prog. Energy Combust. Sci. 20, 203-279.

Luque J. and Crosley D. R., 1999, "Lifbase (version 1.6)", computer program by SRI International, SRI report No. MP 99-009.

Rothe E. W., An H., Hitchcock L. M., Gu Y., and Reck G. P., 1996, "Rayleigh and predissociative fluorescence imaging of densities from an internal combustion engine using a tunable KrF laser", Laser Applications in Combustion and Combustion Diagnostics II, R. J. Locke, ed., Proc. SPIE 2122, 79-82.

Rothe E. W., and Andresen P., 1996, "Application of tunable excimer lasers to combustion diagnostics: a review", Applied Optics Vol. 36, 3971-4033.

Stocker R., Karl J., and Hein D., 2000, "Fluorescence spectroscopic measurements in methane/air and hydrgen/oxygen atmospheric pressure flames in the excitation wavelength range of 303 nm to 240 nm ", 10th Int. Symposium on Applications of Laser Techniques to Fluid Mechanics, Lisbon, Portugal.

Versluis M., Boogaarts M., Klein-Douwel R., Thus B., deJongh W., Braam A., ter Meulen J. J., Meerts W. L., and Meijer G., 1992, "Laser-induced fluorescence imaging in a 100 kW natural gas flame", Appl. Phys. B 55, 164-170.

Versluis M., Queeney K. L., Springfield J. L., Dreier T., and Dreizler A., 1994, "Laser-induced fluorescence detection of OH in a flame near 268 nm", J. Mol. Spectrosc. 166, 486-488.

